

Supplementary Materials for

The target landscape of clinical kinase drugs

Susan Klaeger, Stephanie Heinzlmeir, Mathias Wilhelm, Harald Polzer, Binje Vick, Paul-Albert Koenig, Maria Reinecke, Benjamin Ruprecht, Svenja Petzoldt, Chen Meng, Jana Zecha, Katrin Reiter, Huichao Qiao, Dominic Helm, Heiner Koch, Melanie Schoof, Giulia Canevari, Elena Casale, Stefania Re Depaolini, Annette Feuchtinger, Zhixiang Wu, Tobias Schmidt, Lars Rueckert, Wilhelm Becker, Jan Huenges, Anne-Kathrin Garz, Bjoern-Oliver Gohlke, Daniel Paul Zolg, Gian Kayser, Tonu Vooder, Robert Preissner, Hannes Hahne, Neeme Tõnisson, Karl Kramer, Katharina Götze, Florian Bassermann, Judith Schlegl, Hans-Christian Ehrlich, Stephan Aiche, Axel Walch, Philipp A. Greif, Sabine Schneider, Eduard Rudolf Felder, Juergen Ruland, Guillaume Médard, Irmela Jeremias, Karsten Spiekermann, Bernhard Kuster*

*Corresponding author. Email: kuster@tum.de

Published 1 December 2017, *Science* **358**, eaan4368 (2017) DOI: 10.1126/science.aan4368

This PDF file includes:

Supplementary Text Figs. S1 to S10 Captions for Tables S1 to S11 Tables S12 to S17 References

Other Supplementary Material for this manuscript includes the following:

(available at www.sciencemag.org/content/358/6367/eaan4368/suppl/DC1)

Tables S1 to S11

Supplementary Text

Characterisation of cell lines by RNA-seq, deep proteome and kinase enrichment

The four cell lines used in the cell mixture (K-562, MV-4-11, SK-NB-E(2) and COLO 205) were analysed by RNA-seq and transcripts were mapped to the hg37 reference genome. In total, 494 protein kinases were transcribed and mutations were found in 139 kinase genes in at least one of the four cell lines. The analysis exclusively considered indels, non-synonymous, mis-sense and non-sense mutations that resulted in an altered primary amino acid sequence upon translation.

COLO 205, K-562, MV-4-11, and SK-N-BE(2) cells had 73, 71, 61, and 76 mutated kinase genes, respectively (with 16, 16, 11 and 20, respectively, located in the kinase domain). Obscurin and CSNK2A3 had the most mutations in the corresponding gene sequence. All kinases, the number of observed mutations and the mutated sequence are provided in Tables S4 and S5. Mutations that did not meet the applied statistical criteria are not listed. For example, BRAF in COLO 205 cells revealed a heterologous point mutation coding for the BRAF V600E mutation. The underlying sequence data, however, had poor coverage. Only 6 reads were evident at the corresponding transcript site; of which two bore mutations. Therefore, this mutation was excluded from the analysis. Mutations that could not be unambiguously determined by Illumina sequencing were also excluded (such as FLT3 insertion mutations expressed in MV-4-11 cells).

To profile the proteome of the four cell lines, peptides from each cell line were separated into 36 fractions using hydrophilic strong anion exchange chromatography (hSAX) and each fraction was subsequently measured by LC-MS/MS. From the deep proteome analysis, 363 protein kinases were identified that were also present in the RNAseq data. Kinobead enrichment of the four single cell lines resulted in 253 kinases; 251 thereof were also observed by RNAseq and 235 were identified in the full proteome analyses. The total overlap between the three methods was 234 kinases. 19 kinases were detected by both RNA-seq and the Kinobead experiments; but were not identified in the proteome. Additional kinases were identified by more peptides in the Kinobead experiments compared to the proteomes; thus highlighting the effectiveness of chemical (affinity) proteomic approaches for sub-proteome enrichment. On average, 52% of the total MS-intensity in the Kinobead experiments were mapped to kinase peptides (fig. S1E). Four kinases (CAMK1G, STK26, MLK4, POMK) were only identified in the Kinobead pulldowns and the proteome. For these, the read threshold by RNA-seq may have been too low, or the mRNA may have been relatively unstable. RNA-seq exclusively identified 115 kinases. This suggested that either these proteins were not enriched by the Kinobeads and/or not detected by mass spectrometry because of low abundance. Alternatively, these proteins may be unstable (e.g., MAP3K14/NIK) and cannot be detected by standard proteomics. Together, the combined data from RNA-seq, deep proteome, and Kinobeads define the target space of the kinase inhibitors that can be measured in our assay (fig. S1F).

In general, the γ -version of Kinobeads used here can capture a majority but not all kinases present in the cell lysate used. Missing kinases may be found by using a different cell lysate (as demonstrated by the use of CAKI cells for MET inhibitor profiling, fig. S1G) or by the use of a more suitable linkable probe illustrated by the use of immobilized

Omipalisib for mTOR inhibitor profiling (fig. S1H). With regard to sensitivity, the assay works best for affinities below $10 \mu M$ as weaker interactions are prone to losses during the washing process leading to variation in the data. The investigation of interactions below 3 nM (the lowest dose used in this study) is possible by simply adjusting the concentration range used. Please also refer to prior literature on the Kinobead technology(13, 14).

We compared our Dasatinib data to KiNativ's biotinylated acyl phosphate probe profiling data. The obtained K_d values correlate well (R=0.91) for overlapping targets(16). We have previously published a direct comparison of the Kinobead and the KiNativ technologies. This revealed overlapping, but also in part complementary kinome coverage, as the KiNativ technology uses covalent ATP probes(56).

Several groups have compared the various technologies used in the field. Sutherland et al. have shown that hot ATP kinase activity assays correlate reasonably well with KinomeScan binding data(17). In a comparison of the Kinativ technology with activity assays, activity data from recombinant kinases is typically an order of magnitude stronger than their apparent Kd values with the acyl phosphate probe but correlate well with cellular compound activity(16). Another study suggest the use of full length proteins or kinase constructs with additional domains and subunits to improve the agreement between activity and binding assays(18).

Several activity and binding assays studying protein-kinase inhibitor interactions have been published to date. For example, Anastassiadis *et al.* profiled 178 KIs (25 clinical) at a single dose against 300 recombinant kinases(6). *In-vitro* binding assays against 442 recombinant kinases were reported for 72 kinase inhibitors (50 clinical) using 11-fold serial dilutions for K_d determination in a series of papers published by Davis, Karaman and Fabian *et al.*(3, 5, 8). At the time of writing, the LINCS database contained single-dose binding data for 161 KIs (67 clinical) and 440 phage displayed kinase domains or mutants thereof(12) and Elkins *et al.* reported 367 tool compounds screened at two doses against 224 recombinant kinases. However, the here presented study is among the first to systematically investigate a large set of clinical molecules.

Detailed data analysis

Kinobeads workflow: To systematically profile clinical kinase inhibitors, a chemical proteomic approach was employed. Here, affinity capture of proteins on Kinobeads is combined with protein identification and quantitative mass spectrometry. Kinobeads (version γ)(14) are a mixture of five immobilized broad-spectrum kinase inhibitors and enables the enrichment of >300 human protein kinases and approximately a total of 3,000 proteins from cell/tissue lysates. Addition of the free inhibitor to the lysate in increasing concentrations results in competition at the ATP-binding site of the kinases. Thus, a dose-dependent prevention of specific protein kinases binding to the beads can be achieved. At each dose of competing inhibitor (or vehicle), proteins bound to the Kinobeads can be identified and quantified by label-free mass spectrometry. Label-free quantification is based on the fact that the MS intensity of peptides scales linearly with the quantity of the peptide present in the sample. The more protein that is bound by an inhibitor in solution, the less that protein will bind to the Kinobeads. Consequently, the intensity of the respective peptides detected by the mass spectrometer decreases. EC₅₀ values can thus be derived from the relative quantity of each protein per dose of competitor (or vehicle) via a

dose-response plot using nonlinear regression analysis. By multiplying with a correction factor that accounts for the depletion of a protein from the lysate in the Kinobead pulldown (14, 56, 89), the EC₅₀ value for each protein can be converted into an apparent binding constant K_d^{app} . The correction factor is determined by performing a second Kinobead pulldown (with fresh beads) on the supernatant of the vehicle control pulldown. The amount of protein captured in the two pulldowns is then compared/quantified.

Kinobeads data processing: Data processing was performed for each drug separately. Raw MS files of pulldowns for one particular drug and with increasing drug concentrations for one compound were processed together and supplemented with 15 highquality DMSO vehicle controls. In order to reduce missing values (i.e., peptides not selected for tandem MS in each LC-MS/MS analysis), the "match between runs" option of Andromeda/MaxQuant was used. After protein identification and quantification with Andromeda/MaxQuant (see Online Methods for details), the resultant file (proteinGroups.txt) was used for subsequent filtering, normalization and curve fitting. For this purpose, reverse hits and not quantified protein groups in the DMSO control were discarded. To derive relative residual binding intensities (I_{rel}) for each protein group at every concentration, both raw- and LFQ-intensities were normalized against the respective DMSO intensity. Curve fitting was achieved using an internally developed R-script that utilizes the drc-package(55). Briefly, each protein group was individually fitted using a four parameter log-logistic regression model (equation 1).

$$I_{rel}(c) = b + \frac{t - b}{1 + e^{s \cdot (\log(c) - \log(i))}}$$

$$\tag{1}$$

where c is the compound concentration and the four free parameters are the plateau of the fit b (bottom), the maximal residual binding t (top) and the hill slope s of the curve at the inflection point I (EC50). First, I_{rel} values derived from the LFQ intensities were used. If no relative LFQ intensity for a protein group was available (due to a low number of identified peptides) or no curve fit could be derived, the relative raw intensities were used in a second iteration. During this process, a summary file (see fig. S2 as an example) containing all curve-fits was generated. The output also generates a comprehensive csv file containing all the necessary parameters and raw data (see PRIDE upload) required for reproducing the results. These were then used for manual target annotation (see below).

Target selection criteria. Targets were manually annotated. A protein was considered a high-confidence target if the binding curve showed a sigmoidal shape with a dose-dependent decrease in binding to the Kinobeads. Proteins that only showed an effect at the highest inhibitor dose were not annotated as targets. The number of unique peptides and MSMS spectra was also included as target selection criteria. Peptide intensity in DMSO controls and MS/MS data quality was also taken into account. Proteins with low peptide counts, MS/MS spectral counts or MS1 intensity that nonetheless showed a reasonable dose response curve fit were considered as potential targets. In addition, if an inhibitor also interacted with similar kinases (*e.g.*, CDK family) it was also considered as a potential target. Low-confidence targets were excluded from further analysis. Note that for some targets, curve fitting with our data processing pipeline was not possible resulting in no or very high K_d^{app} values. Targets were considered as direct Kinobead binders if

annotated in Uniprot.org as a protein or lipid kinase. Furthermore, nucleotide binders, helicases, ATPases and GTPases, FAD (*e.g.*, NQO2) and heme (*e.g.*, FECH) containing proteins were also considered as potential direct binders. Most other target proteins are interaction partners/adaptor proteins of the kinases and are termed indirect Kinobead binders. A complete annotation of all target proteins is provided in Table S2.

Data availability. Both raw and processed data for each individual drug profile are available in proteomeXchange (http://www.proteomexchange.org, identifier PXD: 005336) and ProteomicsDB (https://www.proteomicsdb.org, identifier: PRDB004257). The processed data consist of the Andromeda/MaxQuant search results and the derived curve fits and are provided as summary pdf and csv files (examples are provided in fig. S2 and Table S2, S3). Briefly, page one of each summary file depicts the core findings visualized as three main elements (fig. S2A). Subsequent pages provide a list of all high-confidence ('*') and low confidence ('#') targets shown in detail and including the elements provided in fig. S2B-D. Proteins that were not annotated as drug targets are provided in a more compact form consisting of the elements shown in fig. S2B-C.

Concentration And Target Dependent Selectivity (CATDS): a versatile scoring system to determine drug selectivity

The large body of data accumulated in this study, enabled us to develop a selectivity metric termed *Concentration and Target Dependent Selectivity* (CATDS) that can be flexibly applied to a range of topics relevant for basic biology, drug discovery and clinical research and application.

Calculation of CATDS. The Concentration and Target Dependent Selectivity (CATDS) measures the engagement of a specific protein target at a particular drug concentration relative to all target protein engagements of that drug at the same concentration. It is calculated by dividing the sum of the target engagements of the target protein(s) of interest by the sum of all target engagements (including target protein(s) of interest) at a particular concentration (equation 2). Target engagement at any concentration can be derived from the dose response curve fits (see formula).

$$CATDS = \frac{\sum (target\ engagement)_{target(s)of\ interest}}{\sum (target\ engagement)_{all\ targets}}$$
(2)

To illustrate the concept, we chose the EGFR inhibitor Gefitinib as an example (see also fig. S3A). The Kinobeads selectivity profile revealed seven target proteins (including EGFR as the most potent target; K_d^{app} of 413 nM). In order to determine the selectivity of Gefitinib for its designated target, EGFR is chosen as the target of interest and CATDS is calculated at the respective K_d^{app} concentration according to equation (3).

$$CATDS = \frac{\sum (target\ engagement)_{EGFR}}{\sum (target\ engagement)_{EGFR,GAK,RIPK2,RIPK3,MET,STK10,FECH}}$$
(3)

The degree of engagement for each target protein is derived from the curve fit at the chosen concentration (here K_d^{app} , fig. S3A). By definition, 50% of all EGFR molecules are occupied with Gefitinib at 413 nM thus the numerator in (3) is 0.5. The denominator is the sum of the target engagements of all seven targets of Gefitinib.

Variations on the CATDS theme for different applications. CATDS can be used to answer a variety of different research question as it can be calculated for a single target protein of interest or groups of target proteins of interest (fig. S3B).

*CATDS*_{target} is calculated by dividing the target engagement of a certain fixed protein of interest by the sum of all target engagements. *CATDS*_{target} is determined for each particular compound at the respective K_d^{app} concentration of the target protein (equation 4). For example, we identified 19 compounds targeting CHEK1 (only 4 of them are designated CHEK1 inhibitors; Fig. 2B). *CATDS*_{CHEK1} was calculated for all 19 inhibitors and Rabusertib was found to be the most selective molecule for CHEK1 in our screen, whereas the RTK inhibitor Sunitinib was the most unselective molecule targeting CHEK1 among 100 other kinases. *CATDS*_{target} can be useful in medicinal chemistry programs or to choose the most selective inhibitor for a biological or biochemical experiment.

$$CATDS_{CHEK1}(Sunitinib) = \frac{\sum (target\ engagement)_{CHEK1}}{\sum (target\ engagement)_{101\ target\ proteins\ in\ total}} \tag{4}$$

*CATDS*_{designated} is calculated by dividing the target engagement of the most potent designated target protein by the sum of all target engagements (fig. S4B, C). The calculation is performed at the K_d^{app} concentration of this particular target (equation 5). For example, AZD-7762 is a designated CHEK1 inhibitor but it has 68 further targets according to our Kinobeads profile. Calculating CATDS_{designated} can help to evaluate the selectivity for the protein which is intended to be inhibited by a certain inhibitor. However, it can also be used to assess selectivity of compounds with different binding modes as exemplified in fig. S4D.

$$CATDS_{designated}(AZD 7762) = \frac{\sum (target \ engagement)_{CHEK1}}{\sum (target \ engagement)_{69 \ target \ proteins \ in \ total}}$$
(5)

 $CATDS_{most-potent}$ is calculated by dividing the target engagement of the most potent target protein of a particular compound by the sum of all target engagements. The calculation is performed at the K_d^{app} concentration of this particular target. The most potent target of an inhibitor is not necessarily the protein an inhibitor was originally designed for. For example, we determined $CATDS_{most-potent}$ to assess the applicability of a compound as a chemical probe (Fig. 2A). KW-2449 targeted a total of 55 proteins and PAK2 was more potently and selectively hit than its designated target protein FLT3 (equation 6).

$$CATDS_{most-potent}(KW\ 2449) = \frac{\sum (target\ engagement)_{PAK2}}{\sum (target\ engagement)_{55\ target\ proteins\ in\ total}}$$
(6)

The application of CATDS is not limited to single proteins but is also applicable for groups of proteins. For this, several proteins of interest are defined as targets and CATDS is simply calculated as the sum of their target engagements divided by the sum of all target engagements. This can be particularly useful if a certain group of proteins should be targeted by a drug (e.g. two functionally important kinases in the same pathway). Furthermore, CATDS could even be used to compare the selectivity of a drug for different modes of actions.

*CATDS*_{multi-designated} is calculated by dividing the sum of target engagements of all designated target proteins by the sum of all target engagements. The calculation is performed at the K_d^{app} concentration of the least potent designated target protein. Many inhibitors are intended to address several target proteins at once (e.g Dasatinib targeting BCR-ABL and SRC) and thus, selectivity for the intended use of that compound should consider all designated targets (equation 7) relative to all 66 targets of this compound.

$$CATDS_{multi-designated}(Dasatinib) = \frac{\sum (target\ engagement)_{ABL1,SRC}}{\sum (target\ engagement)_{66\ target\ proteins\ in\ total}} \quad (7)$$

 $CATDS_{MoA}$ is calculated by dividing the sum of target engagements of selected proteins by the sum of target engagements in a (restricted) set of target proteins. The calculation is performed at the K_d^{app} concentration of the most potent target protein of the selected target group as we expect an influence on the respective mode-of-action even if only one member is inhibited. For example, we used CATDS_{MoA} to analyse CDK mode of action (fig. S7C). For this purpose, we selected e.g. CDK4 and 6 (role in cell cycle) vs all CDKs (restricted set, irrespective of biological role) (equation 8).

$$CATDS_{MoA-Cellcycle} \ (Dasatinib) = \frac{\sum (target \ engagement)_{CDK4,CDK6}}{\sum (target \ engagement)_{CDK4,CDK6,CDK9,CDK16,CDK17}} \ (8)$$

In summary, the CATDS approach combines several important aspects of selectivity determination which are not considered in their entirety by other selectivity metrics published so far (fig. S3C). Other selectivity metrics such as the selectivity score, the Gini coefficient, the selectivity entropy and the partition index cover some aspects of selectivity and are applicable for particular questions but comparisons to CATDS show that CATDS is more versatile and outperforms other scores as discussed in the following paragraphs.

CATDS versus selectivity score. Perhaps the simplest way to measure selectivity is given by the selectivity score (3, 5). It is calculated by dividing the number of target proteins of a drug at an arbitrary concentration (say 100 nM) by the number of tested proteins. It ranges from 0 (very selective) to 1 (very unselective). The selectivity score can be used either as a global assessment or for a certain target protein. The drawbacks of this scoring system are clearly the strong dependence on the panel size used for screening and the fact that target proteins are only counted and the experimentally determined target engagements are not considered. This impairs comparability between different screens and reduces the score to a rather imprecise measure of selectivity. For example, a comparison of

CATDS_{designated} and the selectivity score (threshold concentration: K_d^{app} of the most potent designated target) shows that both scores correlate to some extent (fig. S3D). However, the selectivity scores are distributed between 0.3 and 0.003 (from 0.5 to 2.5 in $-log_{10}$ scale) and are therefore not capable of distinguishing well between selective and non-selective compounds. All inhibitors appear to be rather selective (low selectivity score) which is mainly due to the large background set the target profiles are compared to (>300 proteins in the Kinobead assay). The CATDS distribution, however, covers the entire score range (0-1) and adequately reflects different inhibitor selectivity towards their designated targets.

CATDS versus Gini coefficient. The Gini coefficient (19) uses the percent inhibition data at a single inhibitor concentration to calculate the relative inhibition fraction of each target protein. It orders and normalizes the single data points to derive a cumulative fraction inhibition plot which describes the inhibitor's selectivity profile depending on the background set of tested kinases as a Lorenz curve. The Gini coefficient is calculated as the ratio of the area outside this distribution and the complete area, resulting in a value between 0 (unselective; all tested proteins are inhibited equally) and 1 (selective; only 1 target protein). Originally, the Gini coefficient was developed to determine selectivity of compounds tested at single compound concentrations which makes it more vulnerable to technical variation. Moreover, it considers the panel size of tested proteins making it difficult to compare selectivity data between different datasets and also leads to poor performance with very small(21) but also very large screening panels (all values close to 1; all assayed proteins contribute to the calculation). The Gini coefficient does not directly allow calculation of selectivity towards a certain target protein. However, to estimate target-specific selectivity by the Gini coefficient, one could use the K_d^{app} of the protein of interest as a threshold concentration. For example, we compared CATDS_{designated} to the Gini coefficient calculated at the same threshold concentration (K_d^{app} of the most potent designated target). Here, CATDS and Gini coefficient show a clear correlation (fig. S3E). Similar to the selectivity score, the distribution of Gini coefficients also suffers from the large background set of protein. This leads to a compressed scale with values mainly between 0.8 and 1 (from 0.7 to 2.5 in $-\log_{10}(1-\text{Gini})$) which hampers clear differentiation of selective and unselective compounds. The CATDS, however, is neither dependent of the tested panel size nor the threshold concentration and distributes between 0 and 1 enabling comparable determination of compound selectivity.

CATDS versus selectivity entropy. Uitdehaag *et al.* introduced the selectivity entropy(20, 90) to enable global selectivity determination for compounds in order to provide a scoring system that would be more comparable between different selectivity profiling screens. The selectivity entropy assumes that a small amount of drug would distribute in an excess of target proteins according to its K_d value in a Boltzmann distribution. The width of this distribution reflects the different energy states of the compound, thus its selectivity, and can be calculated by theoretical entropy calculation. This scoring system enables the calculation of compound selectivity independent of the tested panel size, yet cannot be calculated at a certain threshold concentration or for a certain target protein. For example, CATDS_{most-potent} can be calculated at the K_d^{app} concentration of the most potent identified target protein in order to provide a view of compound selectivity independent from its designated target protein. CATDS_{most-potent}

(inversely) correlates well with the selectivity entropy (fig. S3F, left panel). In contrast to CATDS, selectivity entropy does not allow determining selectivity of a compound for a particular target protein. Comparison of CATDS_{multi-designated} and selectivity entropy highlights this advantage of CATDS. It reveals that there are compounds with very low selectivity entropy values (allegedly quite selective molecules) but it ignores the possibility that another target is more potently inhibited than the intended target (i.e. the selectivity entropy values are artificially low; fig. S3F, right panel). In contrast, CATDS_{multi-designated} is able to distinguish whether a compound is selective for its intended use (blue) or if another protein is targeted more potently (black).

CATDS versus partition index. Similarly to the selectivity entropy, the partition index(21) is based on the theoretical distribution a compound would have in a complex mixture of protein targets (proteins in excess). The compound will distribute between the protein targets according to its affinity (K_d values) and the partition index describes the relative affinity for a reference kinase compared to all measured affinities. Thus, the partition index is independent of the tested panel size as it only uses targeted proteins for calculation and it can be used to determine selectivity of a compound towards single or groups of proteins. Both, the partition index and the CATDS are based on full dose response data with a thermodynamic background. Indeed, we found that both scoring systems correlate well (fig. S3G) for single (left panel, reference: most-potent target protein) and multiple targets (right panel, reference: multi-designated at K_d^{app} concentration of most potent target). However, one advantage of CATDS over the partition index is that the CATDS calculation accounts for the curve shape of the dose response which is more precise than the K_d^{app} value itself as it considers binding effects that might result in different Hill slopes. In addition, the partition index does not allow for determining drug selectivity at individual drug concentrations which is a clear advantage of CATDS (fig. S3H).

Calculation of CATDSI. As discussed earlier, drug selectivity can vary with increasing drug concentration – a fact which underscores the necessity of calculating the CATDS across the tested concentration range to identify the optimal concentration for maximal selectivity (fig. S3A, lower panel). However, the effect of a drug is determined by the engagement of its target protein(91), as estimated by the dose response curve in this screen. That means, that concentrations below K_d^{app} might result in high selectivity for a certain target, but drug efficacy may be very low. In order to determine the most selective yet effective concentration of a drug, the CATDS can be multiplied with the target engagement at each drug concentration to generate the *Concentration And Target Dependent Selective Inhibition* (CATDSI; equation 9). The maximum of this curve highlights the drug concentration at which the optimal balance between selectivity and potency of a drug for a certain target is reached (Fig. 3A, lower panel, red line).

$$CATDSI = CATDS \times \sum (target\ engagement)_{target(s)\ of\ interest}$$
 (9)

Thermodynamic basis of CATDS. If an inhibitor is added to a pool of target proteins (such as in cells or cell lysates) and the thermodynamic equilibrium is established, the

inhibitor will bind to its target proteins according to the applied drug concentration and the respective binding affinities. We assume that the concentration of each target protein is much lower than the specific dissociation constant of the drug-protein interaction which assures that the actual protein concentration is negligible for the calculation of K_d^{app} values. We also assume that the binding of a drug to its target proteins does not reduce the effective concentration of a drug, ensuring that each individual drug-protein binding equilibrium can be established at the applied drug concentration. Both assumptions are prerequisites for determining binding affinities in a dose response experiment. If these basic assumptions are met, we can derive the relative target engagement of each individual protein at each particular drug concentration directly from its dose response curve (e.g. 50% target engagement if the drug concentration is equal to the K_d^{app}). With increasing drug concentration, more and more protein binding sites will be occupied by the inhibitor and target engagement will eventually reach 100%. This is true for any target protein present e.g. in a cell albeit the concentration at which this happens will be different between proteins as their affinities for the drug are not the same. This has important consequences for determining drug selectivity. For instance, consider inhibitor A that has 1 target with a K_d^{app} of 1 nM, 10 targets with a K_d^{app} of 100 nM and no further targets beyond 100 nM. Then consider another inhibitor B that has 2 targets with a K_d^{app} of 1 nM each and no further targets beyond 1 nM. Both inhibitors have different selectivities depending on the applied drug concentration. Inhibitor A is more selective at 1 nM, whereas inhibitor B is more selective at 100 nM. As a consequence, drug selectivity should generally be determined as a function of the inhibitor concentration. Yet, this is very often not done in drug research.

Notes on CATDS for Kinobeads data. The target space of a drug is dependent on the assayed proteins. In this study, we identified >300 probable direct binders to Kinobeads including kinases and other ATP or cofactor binding proteins (Table S2). All these were taken into account when calculating compound selectivity. In contrast, proteins not classified as direct binders (e.g. complex partners) were not considered for selectivity calculation. In Kinobeads experiments where native cell lysate is used for measuring drug-protein interactions, we observed a bottom plateau for some targets (i.e. dose response curve not reaching zero despite high compound dose). Also, we observed that the vehicle control did not necessarily start at 1 which is usually due to technical reasons, for instance if the DMSO control used for normalization showed low MS intensity. Therefore, dose response curves were bottom and top corrected to enable use of the full effect size range between 0 and 1.

CATDS turns out to be a very versatile and practical, yet simple to calculate, scoring system for the determination of compound selectivity. It can use various input data formats (activity or binding, single dose or full dose response). CATDS is also flexible in terms of choice of which set of proteins or drug dose is used in the calculation. Therefore, it can be applied for asking very different questions regarding compound selectivity. Kinobeads data appears to be particularly amenable to CATDS because the experimental setup of using native cell lysate comprising a very complex mixture of endogenous proteins at vastly varying concentrations approximates the dose dependent binding behavior of a drug within a native cellular environment and which directly reflects the underlying thermodynamic equilibrium.

Characterization of Dabrafenib off-targets

For Dabrafenib, the Kinobeads data showed potent binding inhibition for CDK2 but no co-competition of any of the canonical cyclins for CDK2 (CCNA2 or E1 or E2). Interestingly, commercial kinase assays using CDK2 did not show any inhibitory effect of Dabrafinib on CDK2 when tested in combination with CCNA2, E and O implying that either the drug can bind the free kinase in cells or lysates without the need for a cyclin or that an hitherto undetected CDK2/cyclin complex exists which is not part of classical assay panels (fig. S5F, Table S12). Unfortunately, we have not been able to test this hypothesis systematically owing to the lack of appropriate reagents.

SIK2 inhibition induces anti-inflammatory response in LPS-stimulated macrophages

The biological function of salt-inducible kinase 2 (SIK2) is slowly being uncovered and reveals a potential role of SIK2 in oncology as well as immune disorders. Recent studies imply a role for SIK2 in the regulation of inflammatory response of the innate immune system(28, 29, 92-94). It was shown, that SIK2 phosphorylates CREB-regulated transcription coactivator 3 (CRTC3) on multiple sites which leads to recognition and thus inactivation of CRTC3 by 14-3-3 proteins(28). In its non-phosphorylated active form, CRTC3 binds and activates the cyclic AMP-responsive element-binding protein 1 (CREB1) which leads to translocation into the nucleus where the transcription factor can then exert its action and regulate gene expression. The exact function of CREB is controversially discussed but it was found that CREB1 is regulating pro-inflammatory responses by inducing the expression of anti-inflammatory cytokines such as interleukin-10 (IL-10). IL-10 modulates the response of effector cells of the innate immune system (such as dendritic cells or macrophages) towards an anti-inflammatory phenotype through down-regulation of pro-inflammatory cytokines like tumor necrosis factor alpha (TNF α). Inhibition of SIK2 by small molecule kinase inhibitors was shown to reduce CRTC3 inactivating phosphorylation and to mediate the up-regulation of CREB-mediated antiinflammatory response characterized by increased IL-10 and decreased TNFα secretion(28, 29, 94, 95).

In our screen, 21 of 243 clinical small molecule kinase inhibitors showed off-target SIK2 inhibition with affinities of below 500 nM. None of these inhibitors were developed for SIK2 and 11 of those inhibitors were not reported to target SIK2 in the literature so far. Biochemical activity assays using a FlashPlateTM-based radiometric assay (ProQinase, Freiburg) confirmed inhibition of SIK2 enzymatic activity for the 11 newly identified SIK2 inhibitors in comparison to the SIK tool compound HG-9-91-01(28). This molecule is commonly used as tool compound to abrogate SIK activity but comprises a rather promiscuous target profile as revealed by LINCS and Kinobeads selectivity profiling (fig. S6E).

To evaluate the biological effect of the 21 identified SIK2 inhibitors, murine bone-marrow derived macrophages (BMDM) were treated with increasing drug doses (8 doses between 1-10,000 nM) and subsequently stimulated with LPS to induce TLR4 mediated pro-inflammatory response (characterized by increasing TNF α levels). Most inhibitors

(13/21) showed down-regulation of TNF α levels with increasing drug concentrations, four inhibitors were not effective and another four inhibitors showed cytotoxic effects. 13 inhibitors that showed TNF α reduction were additionally examined for their effect on IL-10 secretion. Up-regulation of IL-10 was detected for most inhibitors and was in general in concordance with TNF α reduction (fig. S6B). A biological replicate with BMDM cells from a second mouse showed distinct absolute values of TNF α and IL-10 but recapitulated the same trends in decreasing TNF α and increasing IL-10 secretion, as exemplarily shown for the compounds HG-9-91-01, UCN-01, AZD-7762, Crenolanib, BMS-690514 and PF-03814735 (fig. S6B). Noteworthy, the novel SIK2 inhibitor UCN-01 revealed pronounced effects on TNF α reduction in the same nanomolar range (EC₅₀ 22 nM) as the tool compound HG-9-91-01. Another already described SIK2 inhibitor, AZD-7762, was less potent (EC₅₀ 124 nM) in inhibiting TNF α secretion, but was found to be the most selective SIK2 inhibitor (CATDS_{SIK2}: 0.216) in our panel of 22 SIK2 compounds (including HG-9-91-01). All inhibitor data and raw data can be found in Table S8.

Cytokine secretion is a rather complex phenotype and involves the activity of several kinases which might also be targeted by the tested inhibitors. Thus, measuring TNF α and IL-10 response is not sufficient to prove SIK2 target engagement in living cells. In order to evaluate whether SIK2 inhibitors identified in our screen are able to perturb SIK2 signaling in a living system, we tested a sub-selection of six SIK2 inhibitors for their ability to down-regulate the phosphorylation status of the SIK2 substrate CRTC3. Therefore, we treated murine bone-marrow derived macrophages at an optimal dose at which we observed pronounced TNF α reduction but no toxic effect on cell viability. SIK2-mediated phosphorylation of CRTC3 S62 and S370 was detected by a parallel reaction monitoring (PRM) mass spectrometry readout(31) (fig. S6C, D). Our results showed clear reduction of the phosphorylation levels of CRTC3 S62 and S370 in comparison to the vehicle control by all tested inhibitors (300 nM HG-9-91-01, 300 nM AZD-7762, 300 nM PF-03814735, 100 nM UCN-01, 300 nM Dasatinib, 1000 nM AT-9283). Both phosphorylation sites showed the same effect upon drug treatments, demonstrating with high confidence that these inhibitors are indeed capable of engaging SIK2 in living cells.

As already mentioned, cytokine secretion is the result of manifold stimuli and the interplay of multiple signaling pathways within the cell. Thus, the observed anti-inflammatory response may not only be due to SIK2 inhibition but also due to the inhibition of other kinase targets. In order to be able to distinguish truly associated targets with TNF α production and to confirm the effect of SIK2 inhibition, we compiled a list of proteins that are members of known pathways in the TNF α production from the literature. The aim was to select additional kinase inhibitors such that the targets associated with TNF α production can be well distinguished. To select as little additional kinase inhibitors as possible, we employed a greedy search algorithm. Briefly, in each step, one extra kinase inhibitor was added to the currently selected inhibitor set (initially 21) which maximizes the heterogeneity of target space. For this purpose, the heterogeneity of the target space is defined as

$$h = w * E$$

, where w is the sum of the maximum pair-wise difference of all pairs of targets, defined as $w = \sum_{i,j,i < j} w_{ij}$, where $w_{ij} = D(x_i,x_j)$, x_i and x_j are the pK_d^{app}s of target i and target j across the inhibitor panel. D is a function calculating the maximum pair-wise difference between x_i and x_j .

E is the pseudo-shannon entropy, defined as $E = -\sum p_t \ln p_t$, where for the *t*th pair of i and j $p_t = w_{ij}/w$. Therefore, a high *w* indicates there is a high overall difference in K_d^{app} s between all pairs of targets and a high E indicates the difference is rather averaged across different pairs of targets, i.e. not driven by the difference of a single pair of targets. The greedy search is stopped when no more target pairs could be separated, defined by $D(x_i, x_j) > 1$. As a result, nine extra inhibitors (PH-797804, GSK-2110183, GSK-690693, GDC-0994, Trametinib, Uprosertib, Abemaciclib, Cobimetinib and Ponatinib) were selected and additionally tested for TNF α response (Table S8). Unfortunately, Ponatinib failed due to technical reasons which lead to a final number of eight additional inhibitors.

In order to evaluate the role of SIK2 in relation to the TNF α production, we used a similar "target deconvolution" approach originally proposed by Gujral et al (30). In short, this method utilizes an elastic net model to predict a polypharmacology-driven phenotypic readout with given inhibition data. During this process, the elastic net model automatically selects features associated with the phenotype. In this study, we used the target space of 26 kinase inhibitors, 18 of which were part of the initially tested 22 inhibitors (TG-100572, AZD-7762, PF-03814735, UCN-01, Crenolanib, Dasatinib, AT-9283, PF-477736, BMS-690514, Milciclib, TAK-901, Nintedanib, ASP-3026, Cerdulatinib, Bosutinib, SCH-900776, XL-019, HG-9-91-01, four cytotoxic drugs were excluded) and 8 additional inhibitors (PH-797804, GSK-2110183, GSK-690693, GDC-0994, Trametinib, Uprosertib, Abemaciclib and Cobimetinib), as input to predict TNFα production in bone-marrow derived macrophages (BMDM). We observed that a clear effect on TNFα production was visible on average around 300 nM while cell viability was not affected at this concentration (Fig. 3C, left panel). Therefore, our analysis mainly focused on dosages of 100 to 300 nM. To evaluate the selection stability of a target at each dose, we generated 100 bootstrap samples and fed them into elastic net models. The result is summarized by two values, namely the selection frequency and the effect size (Fig. 3C, middle panel). Our analysis revealed that SIK2 is the most frequently selected target and has the largest effect size in comparison to other targets that have similar selection frequency (e.g. CHEK1). The results confirmed our hypothesis that a decrease in TNFa production can be initiated by the inhibition of SIK2. Other kinases that may affect TNFα response in our inhibitor set include CHEK1, PDPK1, MAP3K11, ZAK and MARK4. CHEK1 was reported to modulate NF-κB signaling(96) by phosphorylating the RelA (p65) NF-κB subunit (pT505). In an oncology background, this phosphorylation was found to correlate with the inhibition of NF-kB target gene expression(97). However, it remains to be investigated how this CHEK1-mediated phosphorylation influences NF-κB activity, and TNFα secretion in particular, in immune regulatory cells. Another interesting target is PDPK1 which has been shown to down-regulate NF-κB signaling in LPS-stimulated macrophages through the PI3K/AKT signaling pathway(98). However, the literature is not clear in this regard as there are other reports that conclude that CHEK1 and PDPK1 inhibition would increase TNFa production. There is also a possibility that the selection of CHEK1 and PDPK1 by the elastic net are due to a technical artifact. This remains to be investigated by e.g. further experiments using highly selective inhibitors (e.g., Rabusertib for CHEK1) which may help to shed light on the influence of these particular protein kinases on TNFα secretion.

Our data confirms previous findings that SIK2 inhibition is a valuable concept to modulate the innate immune response to an anti-inflammatory phenotype. We extended the landscape of SIK2 inhibitors landscape by 11 compounds and provide bioactivity data

for 21 SIK2 inhibitors of which most have not been characterized in that way so far. Especially, UCN-01 and AZD-7762 were found to elicit a distinctive anti-inflammatory response (TNF α reduction, IL-10 increase) and might thus be interesting candidates for further investigation.

Saracatinib affects osteosarcoma cells by dual inhibition of SRC and BMP receptor signaling

Saracatinib was developed as a dual SRC/ABL inhibitor(99) and has been subject to 33 clinical trials so far. Amongst other diseases and other cancer entities, Saracatinib is currently also evaluated in two phase 2 clinical studies investigating a therapeutic effect of this drug on osteosarcoma (NCT00752206) and bone neoplasms (NCT00558272). The potential therapeutic effect of Saracatinib on osteosarcoma was so far mainly attributed to the inhibition of its main target SRC, which was found to play an important role in bone sarcoma cell survival(100, 101). Target profiling using the Kinobeads technology confirmed that Saracatinib not only targets SRC and ABL as previously anticipated but also a whole range of BMP receptors (BMPR1A, ACVR1, ACVR1B) with high affinities(102). The exact role of BMP signaling in osteosarcoma is controversially discussed in the literature, but several studies correlated BMP signaling in osteosarcoma to pro-migratory and metastatic effects as well as poor survival (103). We therefore hypothesized that Saracatinib might affect osteosarcoma cells in a dual mode-of-action by inhibiting both, SRC and BMP signaling. To investigate this hypothesis, we selected the human osteosarcoma cell line U-2 OS and performed drug treatment with cell viability and phosphorylation status readouts as well as protein knockdown experiments.

Saracatinib treatment inhibited U-2 OS cell viability with higher potency than the unrelated ovarian cancer cell line NCI/ADR-RES which was characterized by relatively low expression of BMP receptors (fig. S6G). Additionally, siRNA-mediated protein knockdown experiments were performed in order to distinguish the influence of single Saracatinib targets (SRC, BMPR1A, ACVR1, ACVR1B) on U-2 OS cell viability (fig. S6G). Knockdown of these kinases resulted in clearly diminished cell viability in U-2 OS while NCI/ADR-RES cell viability was affected to a much lower extent. Knockdown of BMP receptors caused similar reduction of cell viability as a knockdown of SRC kinase, further substantiating the dependence of U-2 OS cells on intact BMP signaling. In order to investigate whether Saracatinib is indeed capable of interrogating both signaling axis within the living cells, we performed drug treatment on U-2 OS cells and examined its effect on the phosphorylation of the BMP receptor downstream substrate SMAD1/5/9 (pS463/465/467, fig. S6H) and SRC autophosphorylation (pY416, fig. S6I). Increasing concentrations of Saracatinib lead to a decrease of both, pSMAD1/5/9 and pSRC, in a dose-dependent manner. The inhibitors Dasatinib and Gilteritinib were used as controls to ensure that the effect on pSMAD and pSRC was not affected by crosstalk between both pathways. Dasatinib is a SRC inhibitor which does not target BMP receptors; accordingly SMAD phosphorylation was not affected by Dasatinib treatment. As expected, Dasatinib showed strong effect on SRC autophosphorylation. Gilteritinib is a multi-target inhibitor which -according to our data - targets BMPR1A and ACVR1 but not SRC. Unfortunately, this inhibitor control was not as conclusive as anticipated as it did not succeed in abrogating SMAD1/5/9 phosphorylation. This might be due to lower affinities

towards BMP receptors in comparison to Saracatinib or due to the fact that one of the evaluated BMP receptors, ACVR1B, was not found to be inhibited by this compound which might reduce the anticipated effect on SMAD phosphorylation. Nonetheless, our data revealed that Saracatinib engaged and perturbed both signaling pathways in human osteosarcoma cells and that both, SRC and BMP signaling, play a pivotal role for U-2 OS cell viability. Thus, simultaneous targeting of both pathways by Saracatinib may provide a valuable strategy for treating bone cancer. Potent inhibition of BMP signaling by Saracatinib may even be exploited for the treatment of other skeletal disorders such as fibrodisplasia ossificans progressive (FOP) where abnormal activation of ACVR1 leads to a constant rigidification of the skeleton.

Phosphoproteomic analysis of EGFR/ERBB2 signaling

Global phosphoproteomic analysis after short-term exposure of BT-474 breast cancer cells to five different EGFR/ERBB2 inhibitors revealed a core set of commonly regulated phosphorylation sites. In addition to the target binding data obtained by the Kinobeads assay, such analysis enables the investigation of inhibitor action directly in living cells. Indeed, the data contains several known and new observations which collectively can help to explain how inhibition of EGFR/ERBB2 translates into decreased cellular proliferation and cytotoxicity. For example, our analysis confirms the known inhibition of the RAF/MEK/ERK and the PI3K/MTOR signaling axis which for instance causes cell cycle arrest (e.g. via de-phosphorylation induced nuclear export of the MAPK1 substrate and transcriptional repressor ERF)(104, 105) (Fig. 4C; fig. S8C-G). Our data also show that phosphorylation of the activity regulating site pS703 of the Na+/H+ antiporter SLC9A1 is strongly decreased in response to treatment with all five inhibitors. SLC9A1 deletion has been described to drastically reduce tumour growth (106) which is why it is tempting to speculate that the observed de-phosphorylation induces SLC9A1 inactivation. Disruption of pH homeostasis may therefore play an important role in mediating cytotoxic effects of the studied inhibitors. Importantly, our data also suggest the involvement of many other phosphoproteins which have not been described so far in this context. For example, it has been very recently shown that FOXK2 inhibits the proliferation and invasion of breast cancer cells and suppresses the growth and metastasis of breast cancer (107). We find that treatment of breast cancer cells induces phosphorylation of FOXK1 pS-436 (average log2FC across inhibitors = 0.84) and FOXK2 pS-424 (average log2FC across inhibitors = 2.16). Although the functional role of those phosphorylation sites is currently unknown, the observed induction of phosphorylation may suggest that both transcriptional regulators may play a role in altering cellular proliferation and invasion. Further support for the latter comes from an established role of the aforementioned mentioned activation of the SLC9A1 antiporter in invasion and metastasis (108). Strikingly, we also found increased phosphorylation of BAHD1 pS180 (average log2 FC across all inhibitors = 1.52) and ATRX pS594 (average log2 FC across all inhibitors = 1.47). BAHD1 represses several proliferation and survival genes(109) and both BAHD1 and ATRX participate in heterochromatin silencing which has a well-established functional role in cancer progression(108). Hence, altered heterochromatin silencing and concomitant change in transcriptional activity might be one (novel) mode of action of EGFR/ERBB2 inhibitors.

Phosphorylation signatures of individual drug molecules are also of value in order to assess the molecular consequences of e. g. polypharmacology. Rather than looking at the set of commonly regulated phosphorylation sites, a well annotated kinase inhibitor target in combination with phosphoproteomic data can enable the identification of differential inhibitor effects and support the correct interpretation of cellular effects of individual inhibitors. For example, we discovered that de-phosphorylation of pS363 of RIPK2 is not caused by inhibition of EGFR/ERBB2 but rather is a consequence of direct RIPK2 inhibition. A well annotated target space has also retrospective value for other phosphoproteomic studies. The RIPK2 pS363 site has been previously shown to be inhibited in response to treatment of melanoma cells with the kinase inhibitor Vemurafenib. This is in line with the fact that our chemoproteomic data clearly identify Vemurafenib as a potent RIPK2 inhibitor(110). Although this represents only a single example, the combination of the present dataset with a more systematic phosphoproteomic analysis of inhibitor action should uncover many more such associations and greatly support the interpretation of phosphoproteomic experiments.

Non-protein-kinase off targets

As the compounds immobilized on Kinobeads are ATP mimetics, we and others have shown that other nucleotide binding proteins may also specifically bind. The large body of data reported here expands on these prior observations.

The metabolic kinase PDXK has previously been shown to bind Seliciclib (Roscovitine) via the pyridoxal binding site(36). We detected binding of PDXK to the designated PLK1 inhibitor BI-2536 (K_d^{app}= 387 nM), most likely via direct binding to the ATP site of PDXK (fig. S6J). Clinically relevant levels of BI-2536 may therefore interfere with vitamin B6 metabolism and potentially lead to the depletion of pyridoxal phosphate, an essential cofactor in the metabolism of amino acids and neurotransmitters. Moreover, PDXK inhibition might render cancer cells less susceptible to chemotherapy(111). Several KIs were potent binders of the acetyl-CoA dehydrogenases ACAD10 (*e.g.* Alisertib) and ACAD11 (*e.g.* Crizotinib). Little is known about the function of these ACADs, but they presumably play a role in fatty acid metabolism. As ACADs use FAD as a cofactor, the kinase inhibitors likely bind to the FAD site of the enzymes. This may potentially be therapeutically exploited, as tumours can switch to oxidative phosphorylation for energy production under conditions of glucose starvation (fig. S6K)(112).

Insights from co-crystal structures of kinase inhibitors and their targets

NQO2: In order to analyze the binding mode and mechanism of NQO2 inhibition by the kinase inhibitors Crenolanib, Pacritinib and Volitinib, the enzyme was co-crystallized with the compounds and high-resolution structures determined by X-ray crystallography (for data processing and structure refinement statistics see Table S13; PDB codes: 5LBY, 5LBZ, 5LBW for the aforementioned compounds). NQO2 is a homodimer with the two active sites sitting at the interface between the two monomers and each containing a FAD molecule as a co-factor. All three compounds were clearly defined in the unbiased Fo-DFc difference density maps in both pre-formed hydrophobic active sites of NQO2, directly above the isoalloxazine ring of the FAD molecule. The interactions between NQO2 and

the compounds are dominated by pi-stacking interactions between the isoalloxazine ring of FAD and residues lining the pocket (Fig. 3D; fig. S6L). Specificity, in all three cases, is further governed by a hydrogen bond to N161. In the Crenolanib and Pacritinib complexes an additional water mediated hydrogen bond to E193 or Q122 can be observed. In comparison with the previously reported structure of Imatinib bound to NQO2(37) an analogous water-mediated hydrogen bond between Q122 and bridging nitrogen can also be seen (PDB code 3FW1). In addition, M154 forms a sulfur-arene contact (113) to an aromatic ring of the compounds in the NQO2 bound Volitinib and Imatinib structures, which provides a significant amount of stabilizing dispersion energy.

MELK. Little is known about the structure-activity-relationship (SAR) of MELK and its inhibitors as information on MELK as a target and compounds from medicinal chemistry programs focusing on MELK have just begun to emerge in the literature (114-116). Our Kinobeads drug screen can be used as a rich source of molecules for SAR elucidation and identification potential lead structures for future medicinal chemistry campaigns. We identified 16 compounds that target MELK as an off-target and 7 of those drugs bound and inhibited the kinase with sub-micromolar affinity (Nintedanib, PF-3758309, K-252a, Lestaurtinib, CC-401, Defactinib, BI-847325; Fig. 5D, fig. S1D, Table S11). Co-crystallization experiments yielded high resolution crystal structures of the MELK kinase domain in complex with the inhibitors Nintedanib, PF-3758309, K-252a, Defactinib and BI-847325 (fig. S9E; for data processing and structure refinement statistics see Table S14; PDB codes: 5MAF, 5MAG, 5M5A, 5MAH, 5MAI respectively). These compounds comprise a diverse set of different pharmacophores, which enabled the determination of a range of different drug-protein interactions. In addition, Nintedanib and BI-847325 are of particular interest as they share large parts of the molecular scaffold but differ significantly in their binding affinities (53 nM and 918 nM, respectively) and selectivity profiles in the Kinobeads assay. Ligand interaction analysis identified a total of 26 drug-protein interactions which were located at different positions within the ATP pocket (e.g. G-rich loop, hinge region, activation loop, catalytic loop, etc.). We have recently described a classification scheme that categorizes interacting residues according to preferential binding, side chain accessibility/targetability and kinome-wide conservation into the categories of key, selectivity, potency and scaffold residues (46). By applying this classification scheme to the obtained MELK data set, we identified 14 scaffold residues, 5 potency residues, 5 selectivity residues (2 of which are reverse selectivity residues; fig. S9E; Table S11). No key residues could be assigned which is probably due to different factors: i) the number of analyzed crystals is still too low, ii) pharmacophore diversity between the compounds is quite high, iii) affinity of the inhibitors is not extremely high and iv) the intended targets of the inhibitors (VEGFR/FGFR/PDGFR, PAK4, PRKC, MEK/AURK) are structurally very different from MELK. The potency residue Glu57 forms direct interactions to Nintedanib and the potency residue Asn137 to PF-3758309 and K-252a, respectively, which might be responsible for the higher affinity of these compounds compared to Defactinib and BI-847325. Particularly, the potency residue Glu57 appears to have a strong influence when comparing Nintedanib and the structurally similar inhibitor BI-847325. Cocrystal structures of both compounds revealed very different binding modes of Nintedanib (DFG in, Cα helix in) and BI-847325 (DFG in, Cα helix out). The shift of the Cα helix is induced by the more bulky ethylamide substituent of BI-847325 and leads to a disruption of the characteristic salt bridge between Lys40 and Glu57 (salt bridge indicates active kinase conformation) and prevents BI-847325 from establishing an interaction with Glu57 as observed for Nintedanib. This might explain the large affinity difference towards MELK. The five selectivity residues (E15, C70, Y88, C89, E93) could potentially facilitate MELK inhibitor design as exemplified by the direct interactions engaged between Nintedanib and E15 (kinome-wide conservation level: 6%) or K-252a and E93 (kinome-wide conservation level: 15%). The selectivity residues C70 and C89 are readily accessible in the center of the ATP pocket and open up the possibility to design irreversible inhibitors for MELK. Given the low conservation level of both cysteines (C70: 1%, C89: 19%) and the fact that this combination of cysteines is present in only one more protein kinase (TBCK), one can anticipate that such an irreversible inhibitor would not only gain in potency and increase the drug's residence time but also provide selectivity towards MELK.

NSCLC patient analysis

Kinobeads experiments from tumor and nearby normal tissue of 15 lung cancer patients revealed differential expression of several interesting protein kinases (namely MELK, EGFR and DDR1, fig S9A). These candidate proteins were followed up in a retrospective study of 375 patients comprising 186 adenocarcinoma cases and 189 squamous cell carcinoma cases (Table S15). Immunohistochemistry staining suggested that MELK was mainly present in the nucleus (Fig. 5A). Overall, we found overexpression of MELK in 291 of 359 NSCLCs (81%), which correlated with poor prognosis of the NSCLCs (p=0.04). The further analysis revealed that 77.7% (140 of 180) adenocarcinoma and 84.5% (151 of 179) squamous cell carcinoma tissues showed high levels of MELK. However, overexpression of MELK had no impact on survival in adenocarcinoma patients (p=0.7) but significantly correlated with survival in squamous cell carcinoma patients (p=0.02) (Fig. 5B). Staining for EGFR revealed membrane localization of the protein. Overexpression of EGFR in NSCLC had no impact on overall survival (p>0.05). High expression of EGFR in Adenocarcinoma (in 114 of 177) correlated with poor prognosis (p = 0.06) whereas high expression in squamous cell carcinoma (135 of 178) was associated with good prognosis (p = 0.03). According to immunohistochemistry staining, DDR1 was mainly expressed in cytoplasm. High expression of DDR1 (20 of 177) had impact on a good prognosis in squamous cell carcinoma (p = 0.05), whereas no significant correlation with survival could be found in adenocarcinoma or the combined analysis (p>0.05) (fig. S9B-D).

<u>Characterization of the novel FLT3 inhibitor Golvatinib and pre-clinical evaluation of Cabozantinib in mice</u>

FLT3-ITD has been proven to be a therapeutic target in acute myeloid leukemia (AML) (117). In early 2017, the multikinase inhibitor Midostaurin has been approved for newly diagnosed AML in adult patients who are FLT3 mutation positive. Clinial trials have also demonstrated Midostaurin activity in patients with FLT3 wild type, owing to either FLT3 or off-target inhibition(118). We identified 30 targets for Midostaurin in our assay with medium affinity and low selectivity (CATDS_{FLT3}: 0.048) for FLT3, whereas

designated FLT3 inhibitors in clinical trials such as Quizartinib, Crenolanib or Gilteritinib showed higher potencies and selectivity values. Overall, 61 inhibitors were identified to bind to FLT3. According to mRNA sequencing of the utilized four cell lines, FLT3 is mainly expressed in the MV-4-11 cell line, harboring a FLT3-ITD mutation (see above and Table S5) suggesting that these compounds are active against the mutated protein.

This work identified Golvatinib as a new and very affine and reasonably selective FLT3 inhibitor (K_d^{app} : 4 nM, CATDS_{FLT3}: 0.249), whereas Cabozantinib showed favorable selectivity for FLT3 (K_d^{app} : 53 nM, CATDS_{FLT3}: 0.457) compared to its other targets. Cabozantinib is approved for the treatment of medullary thyroid cancer and renal cell carcinoma based on the inhibition of c-MET and VEGFR and appears to be well tolerated. Thus, further repurposing of this inhibitor for other indications might be possible.

We screened a panel of leukemia cell lines against Cabozantinib using the designated FLT3 inhibitors Quizartinib and Crenolanib as positive controls (up to 500 nM *in vitro*). Cell metabolic activity was measured by an MTS-assay. The cell lines THP-1, OCI-AML3, OCI-AML5, U-937, KG-1a, NB-4, HL-60, SD-1, and K-562 were resistant to all three inhibitors. Remarkably, all three compounds inhibited proliferation of cell lines harboring mutations in receptor tyrosine kinase (RTK) class III receptors (PDGFR subfamily, including FLT3) in the low nanomolar range (Table S16, 17). Cell viability for a subset of these cell lines (MOLM-13, MV4-11, MM-6, Kasumi-1, OCI-AML3, HL-60, KG-1a and THP-1 was measured by the trypan blue assay (after 72 h of drug treatment; fig. S10A). To validate FLT3 inhibition by Golvatinib, we also treated MV-4-11, OCI-AML3 and HL-60 cells with the drug. Noteworthy, only cell lines with mutations in the PDGFR-RTK family were sensitive to the drugs, with Golvatinib being the (relatively speaking) least potent one (EC $_{50} = 26$ nM).

We next treated Ba/F3 cells expressing different FLT3 mutants with the three inhibitors and assayed their viability after 72 h (fig. S10B). All three drugs inhibited FLT3-ITD E611C(28) (NPOS) with EC₅₀ values below 40 nM, FLT3-ITD 598/599(22) (w78) below 15 nM and FLT3-ITD K602R(7) (w51) below 10 nM. Among the tested drugs, Quizartinib was the most potent inhibitor, followed by Cabozantinib. All three inhibitors can inhibit the proliferation of cells carrying the resistance mutation FLT3-ITD E611C(28) N676K(119) but only Crenolanib showed an effect against FLT3-ITD E611C(28) D835Y(86). The tyrosine kinase domain FLT3 D835Y mutation alone was also less sensitive towards Cabozantinib treatment. Thus, Cabozantinib was not able to overcome AML-resistance against common treatment options at lower doses. A combination of the N676K and D835Y mutations also renders the Ba/F3 cells resistant towards Cabozantinib, whereas Crenolanib shows the best inhibitory effect on proliferation in these cases. Moreover, all three inhibitors showed an inhibitory effect on KIT expressing cells but with lower potency compared to cells expressing FLT3-ITD mutations (fig. S10B; Table S17). Golvatinib treatment reduced viability of FLT3-ITD K602 (7) cells but had no effect in the Ba/F3 clone with resistance mutation.

Immunoblot analysis of Golvatinib and Cabozantinib in FLT3 wild type or FLT3-ITD transfected HEK293 cells showed that all compounds reduce FLT3 phosphorylation in the mutant and wild type form proving target engagement in living cells (fig. S10C). In FLT3-ITD dependent MV-4-11 cells, lower doses of drug are sufficient for inhibition of FLT3 signaling (fig. S10D).

To determine the effect of Cabozantinib on cellular FLT3 expression levels, U-2 OS cells were transiently transfected with FLT3 wild-type and mutant constructs (FLT3-ITD (K602R(7) (w51), FLT3-ITD E611C(28) (NPOS)). Cells were treated with 50 nM Cabozantinib while control cells were left untreated prior to immuno-fluorescent staining for DNA (DAPI), membranes and other lipophilic structures (WGA) and FLT3. In untreated FLT3 wild type cells, FLT3 is located at the membrane and in the cytoplasm of the cell, whereas the FLT3-ITD mutation leads to an apparent displacement of the receptor from the membrane. Comparison of Cabozantinib treated and untreated controls revealed an increase in FLT3 surface localization, similar to the one previously observed for Quizartinib(120). Therefore, Cabozantinib treatment is able to restore the membrane localization of FLT3-ITD (Fig. 6A; fig. S10E). Furthermore, immunoblot analysis showed that Cabozantinib abbrogated phosphorylation of STAT5 in MV-4-11 cells and thus stopped this aberrant signaling (49). at doses below 10 nM (fig. S10D).

As a result of Cabozantinib treatment efficacy in cells, we next evaluated the drug in a systemic xenograft mouse model of AML. Wild type FLT3 (OCI-AML3) or FLT3-ITD mutated (MV-4-11) cells were injected into the tail vein of NSG mice. Cabozantinib treatment started on day three after cell injection with a dosage of 60 mg/kg (prior dose escalation trials showed no drug related toxicities at this dose). Mice were imaged every four to five days and bioluminescence imaging was used to monitor tumour burden in the animals. Solvent treated control mice showed a high bioluminescence signal starting on day 13 and therefore had to be sacrificed starting with day 17 after cell injection. Cabozantinib treatment was continued until day 14 and was then stopped so that survival could be monitored by Kaplan Meier analysis. After drug treatment was discontinued, cancer cells started growing and luminescence concommittantly increased (fig. S10F shows exemplary mice for disease development). From these experiments we conclude that Cabozantinib treatment leads to a significant reduction of tumour growth in FLT3-ITD positive but not FLT3-WT AML cells. In addition, treatment significantly prolonged the survival of MOLM-13 bearing mice (fig. S10G, H) making Cabozantinib a promising candidate for further evaluation in AML patients stratified for FLT3-ITD.



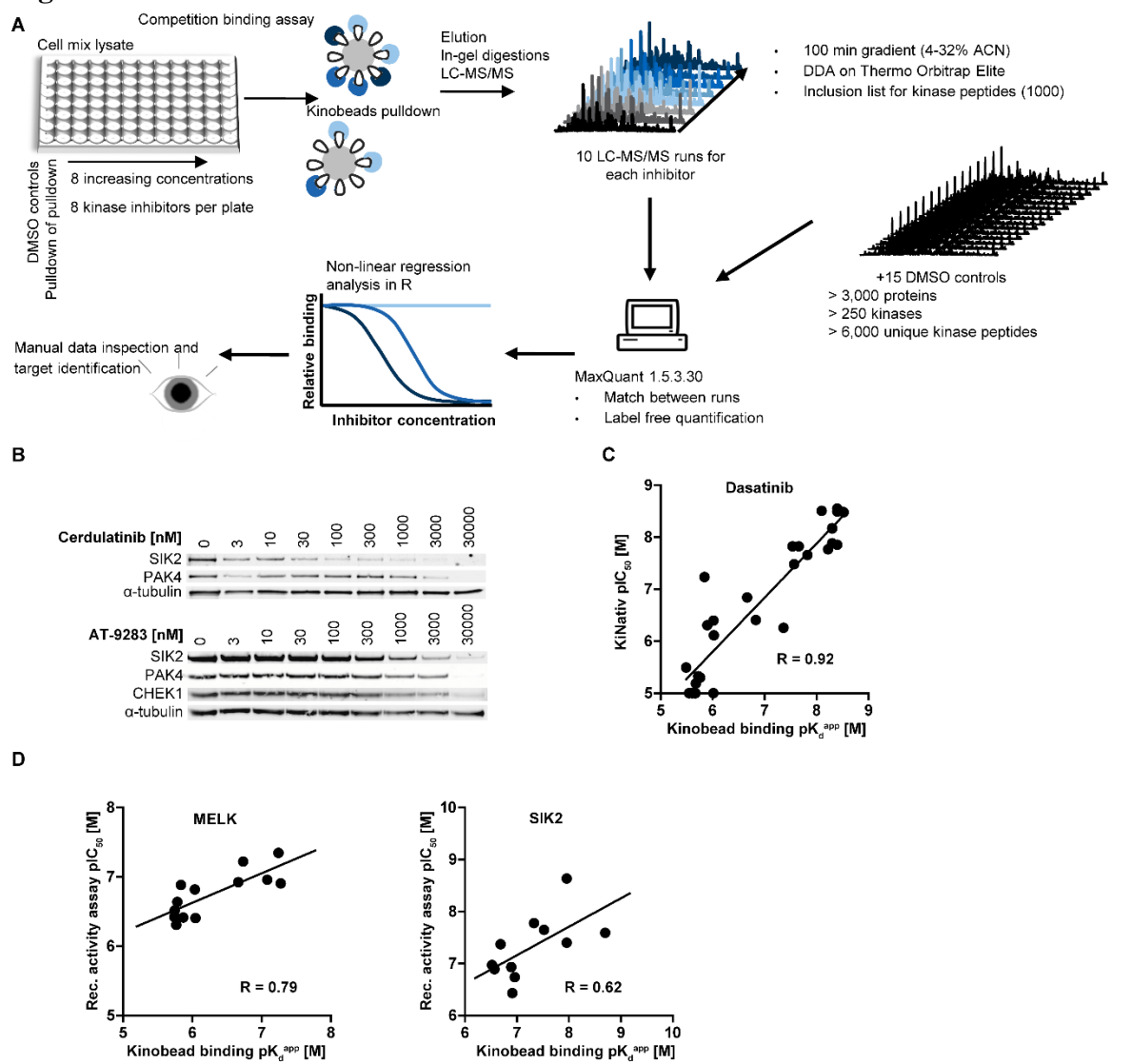


Fig. S1 | **Kinobeads Drug Screen workflow and evaluation.** (**A**) Kinobead pulldowns were performed in 96-well format. Eight doses were used for each drug plus vehicle control and a second pulldown of the vehicle control (pulldown of pulldown). This control was used to correct for protein depletion from the lysate caused by the affinity enrichment (see methods). Proteins were eluted from beads, run ~1 cm into a LDS gel and in-gel digested with trypsin. Each pulldown was analysed by liquid chromatography tandem mass spectrometry and using an inclusion list of kinase peptide m/z and retention times collected in prior experiments. MS data from the same 15 vehicle control Kinobeads pulldowns were added to the MaxQuant/Andromeda software for consistent protein identification and quantification. Dose response plots were generated and target proteins manually annotated. (**B**) Kinobead western Blot readout for selected inhibitor:protein combinations.

(C) Dasatinib target pK_d^{app} correlate well with KiNativ binding data for the same inhibitor.

(D) Correlation of Kinobeads binding data for clinical MELK and SIK2 inhibitors to IC₅₀-values obtained in recombinant activity assays shows reasonable agreement between the two assay formats.

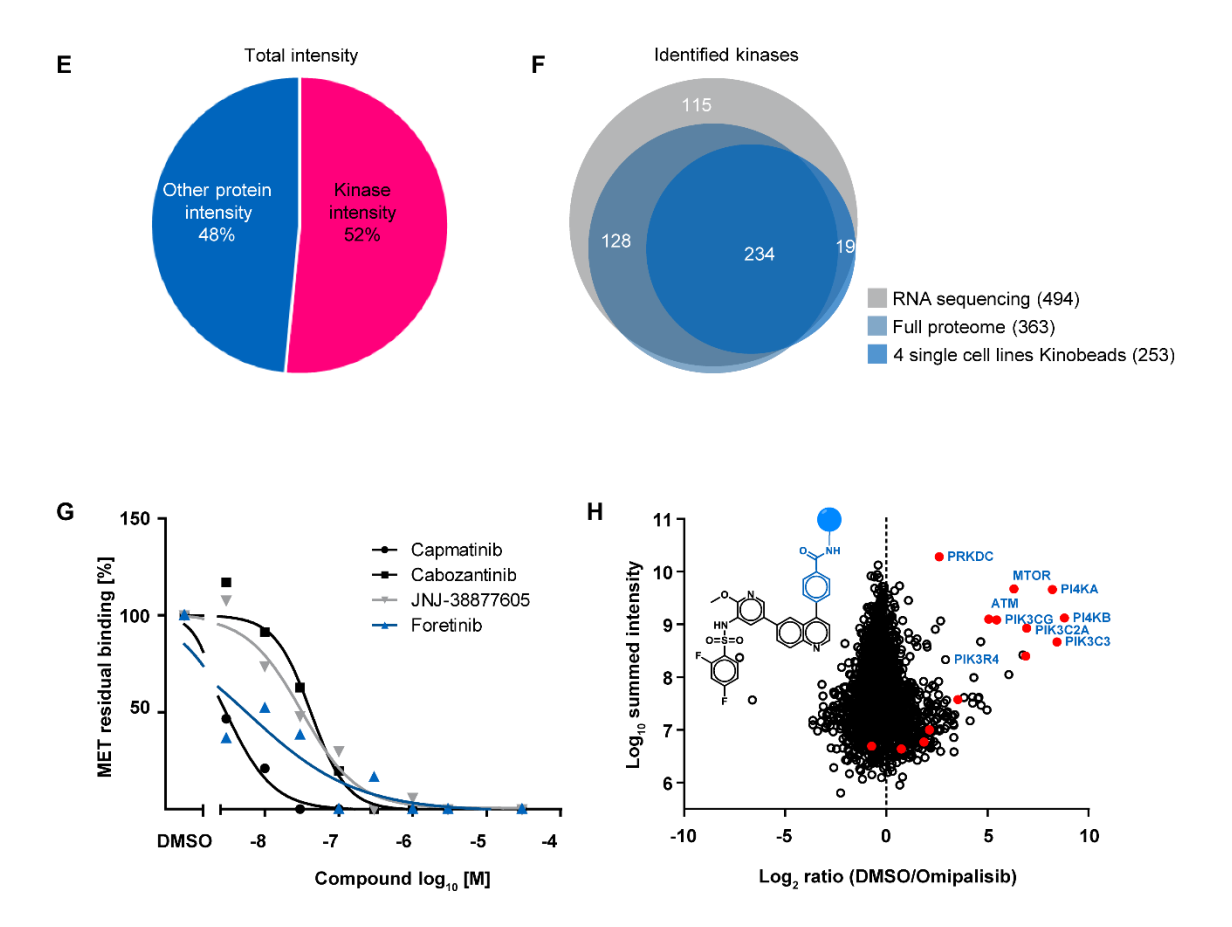


Fig. S1 continued | **Kinobeads Drug Screen workflow and evaluation.** (**E**) Intensity distribution of proteins captured on Kinobeads. From the total MS peptide intensities, 52% originated from kinase peptides illustrating good enrichment of kinases on Kinobeads. (**F**) Venn diagram of the overlap of protein kinases identified in the RNA-seq data, full proteome analysis and Kinobeads pulldowns in K-562, M-4-11, COLO 205 and SK-N-BE(2) cells. (**G**) Examples for Kinobeads experiments performed to profile MET inhibitors using a lysate mixture of the four standard cell lines supplemented with Caki-1 cell lysate (high MET expression). (**H**) Kinobeads competition data for MTOR/PI3K-family members (red) using immobilized Omipalisib (inset) and unmodified Omipalisib as the competitor.



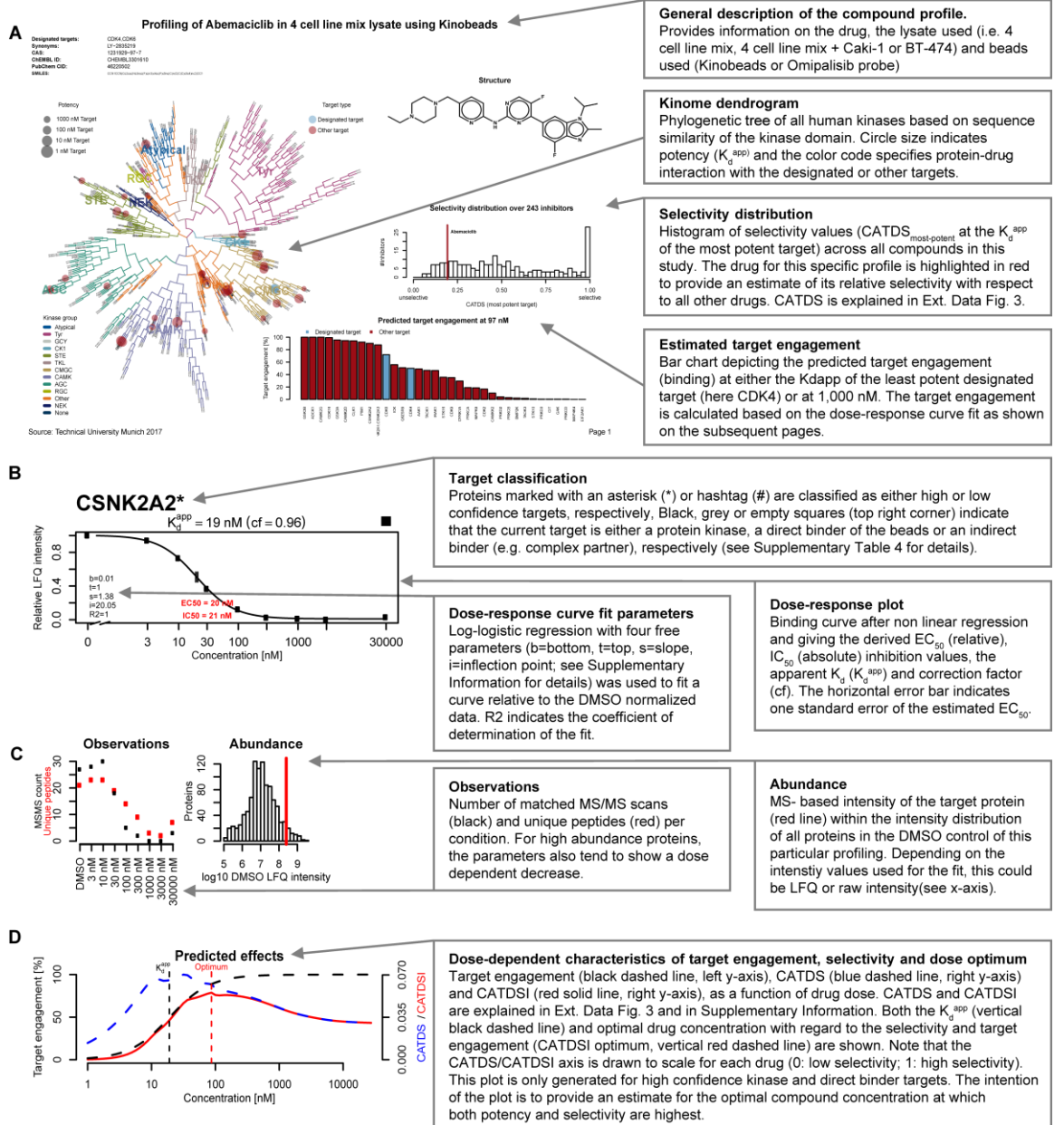


Fig. S2 | **Description of target profile summaries.** For reference purposes, we have created pdf files summarizing the target profiles of all 243 inhibitors used in a total of 281 experiments. (**A**) Page 1 highlights general information about the inhibitor. Each identified target kinase (blue for designated target, red for other targets) is highlighted on the phylogenetic tree of all human kinases. A histogram plot places the inhibitor on the distribution of selectivity of all drugs investigated in this study. The histogram at the bottom of panel (**A**) indicates the level of target engagement of the drug in the cell lysate at a defined concentration. (**B**) Beginning with the high confidence targets, the subsequent pages show all MS intensity-based dose-response profiles obtained for the compound including parameters for curve fitting and derived IC₅₀, EC₅₀ and K_d^{app} values. (**C**) For each protein, further analytical evidence is provided (number of MS/MS scans, number of unique peptides) and how abundant the protein was within the experiment (LFQ or raw intensity in the DMSO control). (**D**) Target engagement, compound selectivity (CATDS) and predicted optimum

of compound selectivity and target engagement (CATDSI) as a function of applied compound dose. The optimum in the CATDSI curve indicates the drug concentration that represents the best compromise between selectivity and target engagement. Visualization information for proteins that do not show dose-dependent binding consists of (B) and (C) only. Links to all target summary files are provided in Table S1. The pdf files can also be retrieved from proteomeXchange and ProteomicsDB (see data availability).



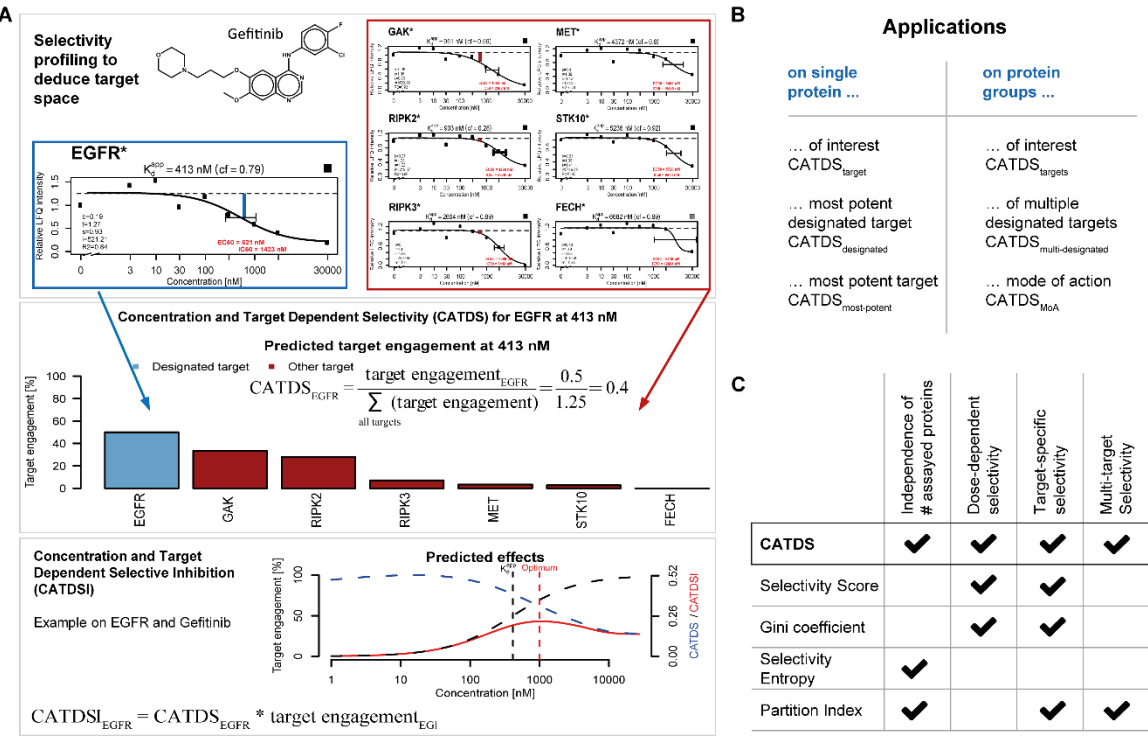


Fig. S3 | Determination of compound selectivity by the Concentration and Target Dependent **Selectivity** (CATDS) score. (A) An example of a CATDS calculation is provided for Gefitinib (upper panel). Kinobeads profiling determined seven targets for Gefitinib (blue box for EGFR and red box for the six other targets). The target engagement (blue vertical bar in the dose-response plot for EGFR; red vertical bar in dose response plot for other targets) is shown for all targets. The histogram in the middle panel uses the same color code. The selectivity of Gefitinib for EGFR (CATDS_{EGFR}) can be calculated by dividing the target engagement of EGFR (here at its K_d^{app} of 413 nM, i.e. 0.5, blue bar) by the sum of all target engagements (blue and red bars) at the same concentration. More generally, using the fitted curves from the Kinobeads assay, CATDS_{EGFR} can be calculated at any concentration (lower panel, blue dashed line) to monitor the selectivity across the entire concentration range. A further useful metric is the Concentration and Target Dependent Selective Inhibition (CATDSI) which provides an estimate of the optimal concentration at which the highest selectivity and highest target engagement can be obtained. Thus, CATDSI_{EGFR} is the CATDS_{EGFR} multiplied by the target engagement of EGFR (lower panel, dashed black line). (B) CATDS can be flexibly used to express the selectivity of a compound for any one protein of interest (CATDS_{target}), one of the designated targets of a compound (CATDS_{designated}) or the most potent designated target of a compound (CATDS_{most-potent}). The score can also be used for protein groups such as multiple target proteins (CATDS_{targets}), multiple designated targets (CATDS_{multi-designated}) or multiple targets involved in a drug's mechanism of action (CATDS_{MoA}). (C) Comparison of CATDS features to four other selectivity measures. CATDS encompasses features of all the other metrics but only CATDS provides an assay-independent selectivity measure for single and multiple proteins of interest at any concentration.

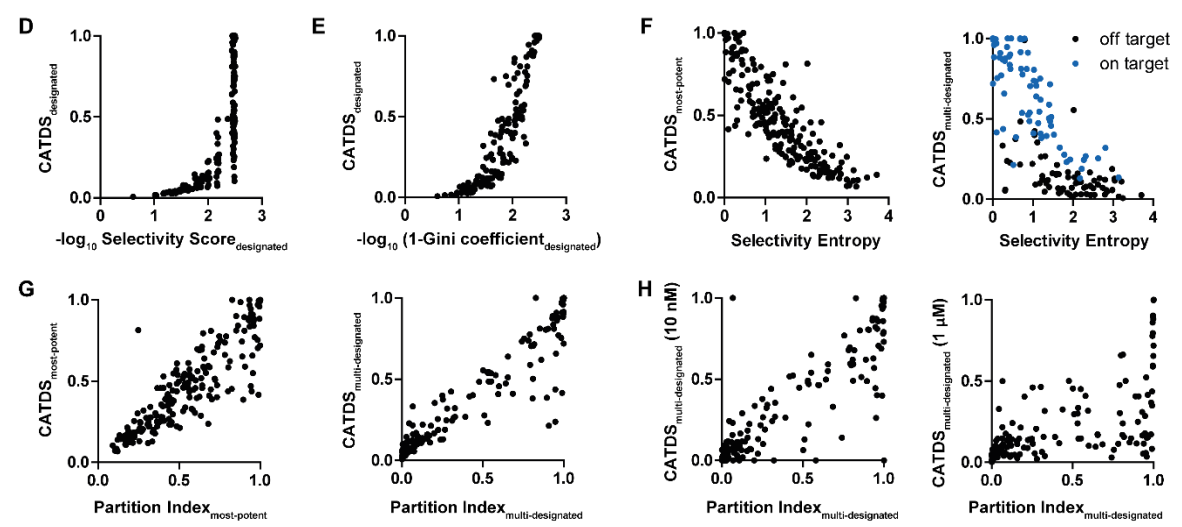


Fig. S3 continued | **Determination of compound selectivity by the Concentration and Target Dependent Selectivity (CATDS) score.** (**D-H**) Generally, there is reasonable agreement of CATDS with four other measures of selectivity. CATDS_{designated} is highly comparable to (**D**) the selectivity score and (**E**) the Gini coefficient. (**F**) Selectivity entropy is comparable to CATDS_{most-potent} (left panel); however, CATDS_{multi-designated} indicates that the selectivity entropy is unable to differentiate compounds that are on-target (blue circles) or off-target (black circles) proteins (right panel). (**G**) There is also a high correlation between CATDS_{most-potent} (CATDS_{multi-designated}) and the partition index_{most-potent} (partition index_{multi-designated}), respectively. (**H**) The comparison of CATDS_{multi-designated} calculated at 10 nM (left) and 1,000 nM (right) with the partition index_{multi-designated} demonstrates that the partition index cannot account for the fact that selectivity is a function of drug dose.

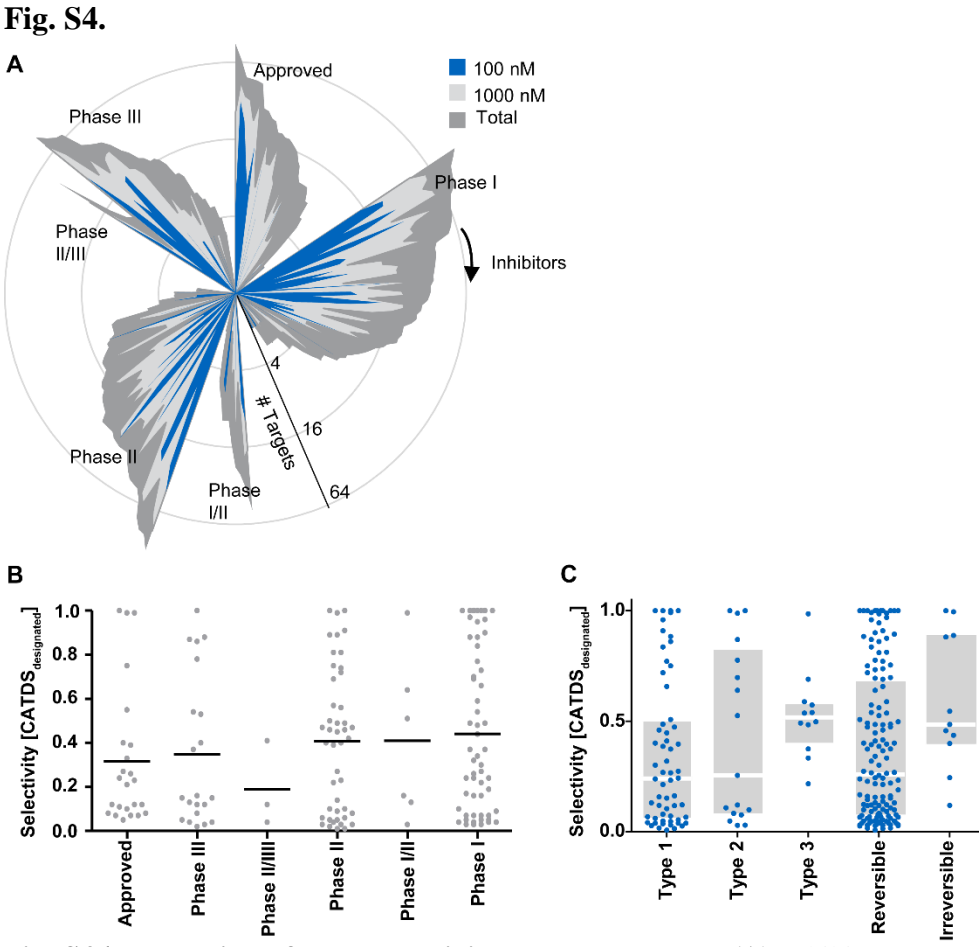


Fig. S4 | **Evaluation of drug selectivity** – **global dataset.** (**A**) Inhibitors grouped by status of clinical evaluation. Given is the number of targets with a potency of below 100 nM (blue), 1,000 nM (light grey) and any concentration (total; dark grey). (**B**) CATDS analysis of drug selectivity according to clinical status (determined from the CATDS for all designated targets at the concentration of the most potent designated target; CATDS_{designated}). There was no difference in selectivity between clinical phases confirming that selectivity is not a strict requirement for progressing a compound in the clinic. (**C**) Selectivity analysis of 137 kinase inhibitors with annotated binding type according to CATDS_{designated} (the most potent designated target of a compound at its K_d^{app}). Type 1 and 2 inhibitors did not differ in median selectivity; while type 3 inhibitors were generally more selective. Irreversible and reversible inhibitors spanned a broad range of selectivity, albeit highly selective molecules were apparent in both.

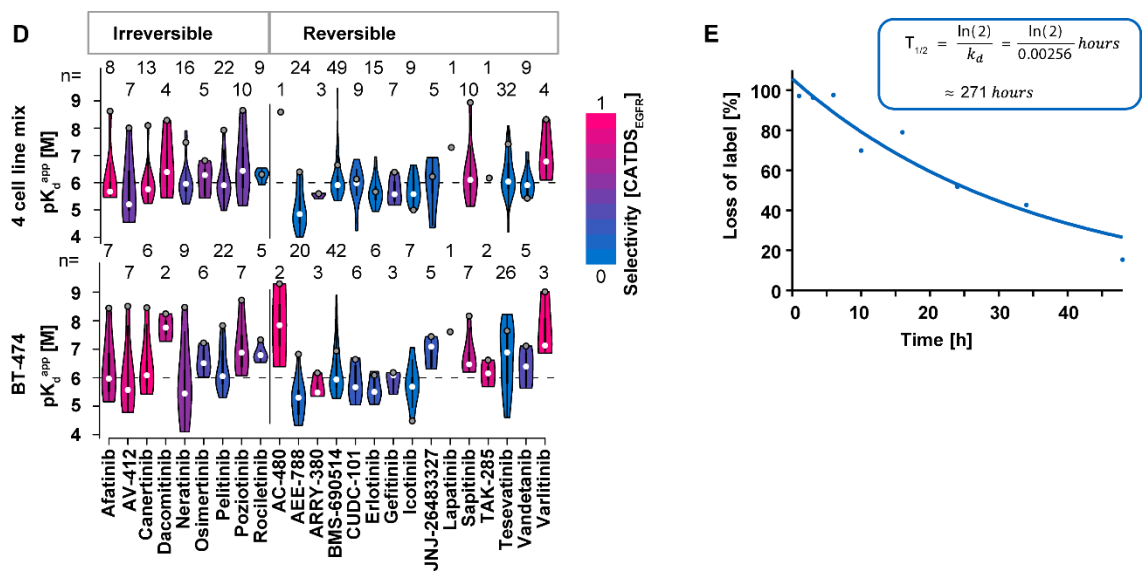


Fig. S4 continued | Evaluation of drug selectivity – irreversible and reversible EGFR inhibitors.

(**D**) Violin plots of EGFR inhibitors profiled in the lysate mixture of the four cell lines (top panel) as well as BT-474 cells (bottom panel). Given are pK_d^{app} values of all high-confidence, direct-binder targets (pK_d^{app} of EGFR highlighted as a grey circle). The shape of the violin indicates the number of targets at the respective pK_d^{app} . The total number of targets is printed at the top (e.g. n=8). Violins are colored according to selectivity for EGFR (CATDS_{EGFR}). (**E**) EGFR turnover measured by pulsed SILAC mass spectrometry and monitoring the loss of a heavy label over time. EGFR turnover was corrected for cell doubling to obtain protein half-lives (see Supplementary Materials).

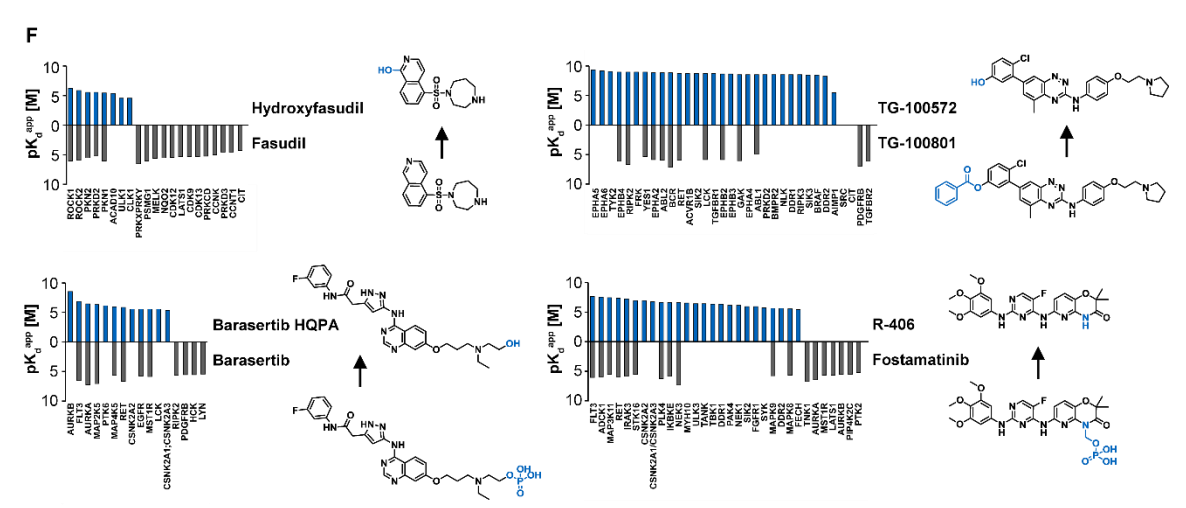


Fig. S4 continued| **Evaluation of drug selectivity. (F)** Kinobeads target profiling data of a prodrug (grey) compared to the active drug (blue) for different compounds that are formulated as prodrugs.

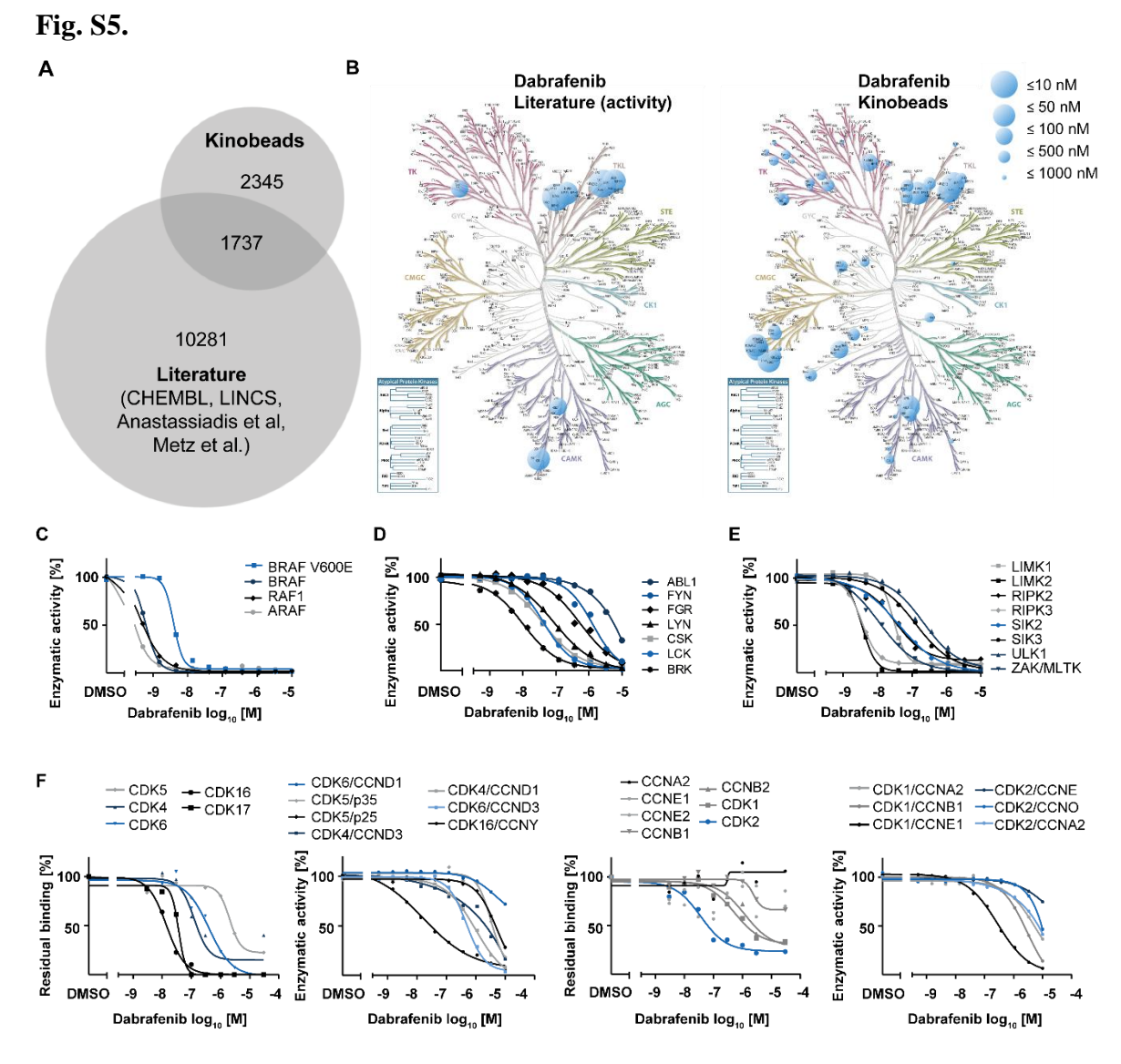


Fig. S5 | **Characterization of novel off-targets.** (**A**) Comparison of protein-drug interactions from this study with those described in major publications and online databases (CHEMBL, LINCS, Anastassiadis *et al.*, Metz *et al.*) (**B**) Phylogenetic tree representation of all human kinases and Dabrafenib targets (blue) determined from activity (left) and Kinobeads binding data (right; illustration reproduced courtesy of Cell Signaling Technology, Inc; www.cellsignal.com). The size of each circle is proportional to the K_d^{app} of the interaction. (**C-E**) Kinase activity assays of novel Dabrafenib targets validated the binding results obtained with Kinobeads. (**F**) Kinobeads binding and kinase activity assays for Dabrafenib and different CDK/Cyclin combinations. Potent binding competition of CDK2 could not be confirmed in the activity assay).

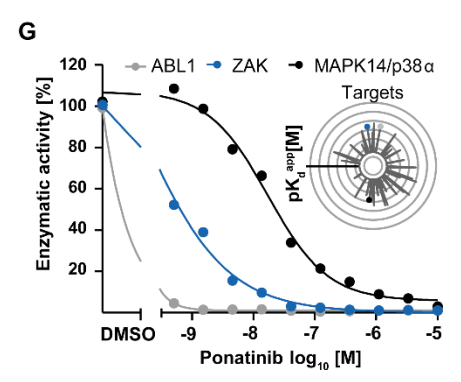


Fig. S5 continued | **Characterization of novel off-targets.** (**G**) Kinase activity assays for Ponatinib and ABL1, ZAK and MAPK14 confirmed that binding data (inserted radar plot for all kinase targets of Ponatinib) translated into inhibition of kinase activity. The target promiscuity of Ponatinib may be responsible for both desired and undesired side effects.

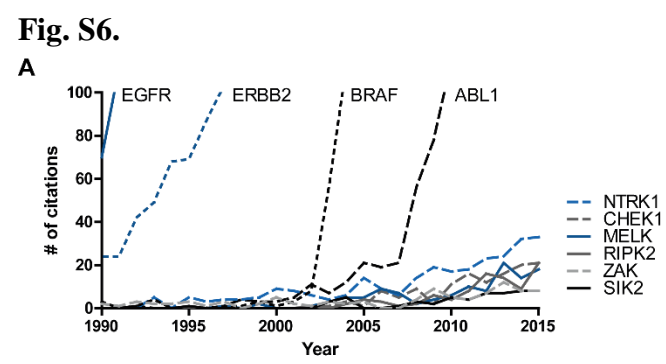


Fig. S6 | **Characterization of novel off-targets. (A)** Citations from PubMed (pubmed.gov, 10/2016) indicating a recent and increasing interest in particular kinases.

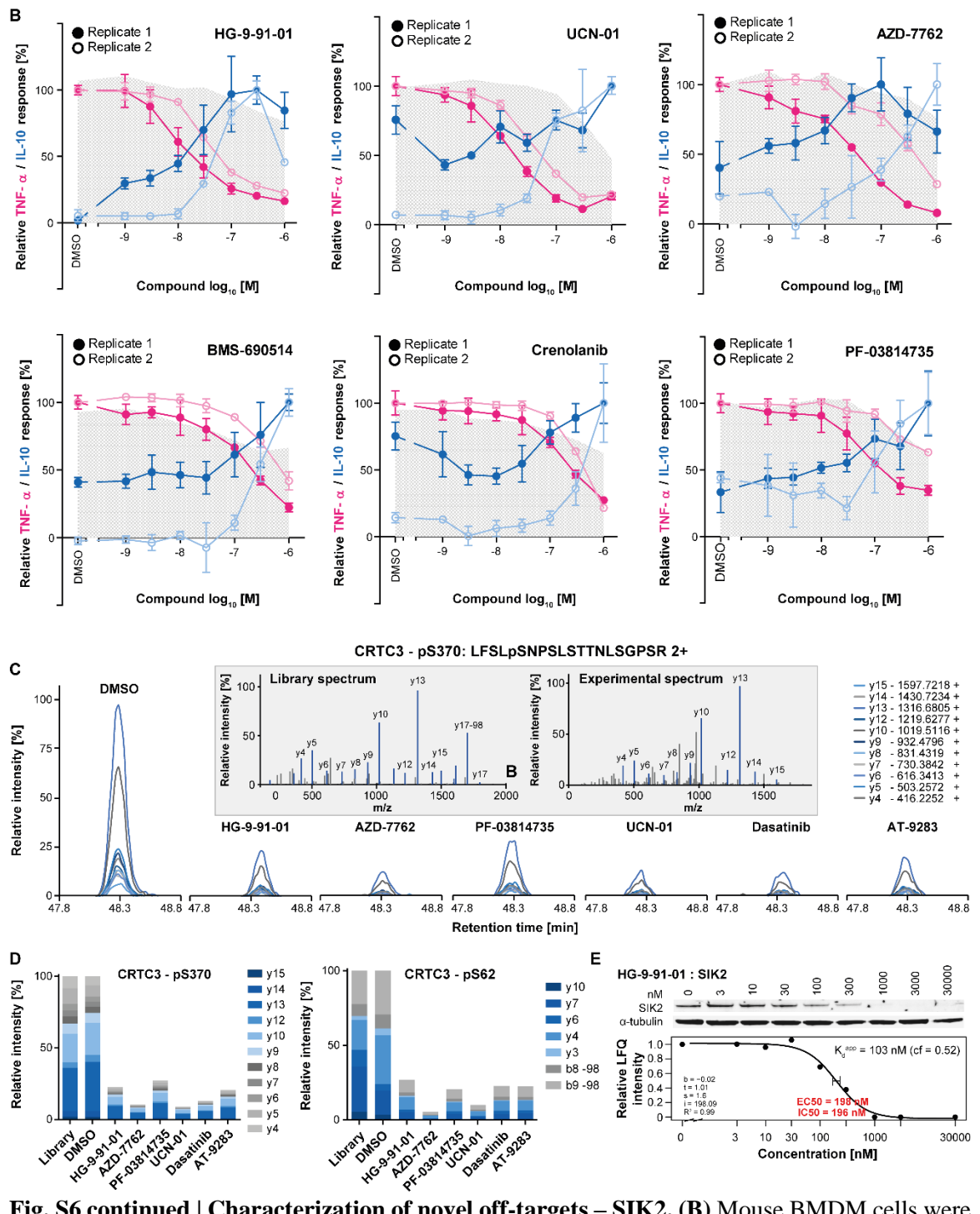


Fig. S6 continued | **Characterization of novel off-targets** – **SIK2.** (**B**) Mouse BMDM cells were treated with increasing concentrations of potential SIK2 inhibitors followed by cell viability (grey area), TNFα (pink) and IL-10 (blue) measurement. All shown inhibitors resulted in anti-inflammatory effects (IL-10 increase, TNFα decrease), suggesting SIK2 inhibition (error bars show standard deviation of technical triplicates). The known SIK2 inhibitor HG-9-91-01 was used as positive control. (**C**) PRM assay for phosphorylation of CRTC3 S370 – a substrate site of SIK2 – showing reduced phosphorylation for all SIK2 inhibitors compared to DMSO. (**D**) Quantitative readout of PRM transitions for either pS370 or pS62 after inhibitor treatment. (**E**) Western blot and mass spectrometry readout of Kinobeads binding of SIK2 by HG-9-91-01.

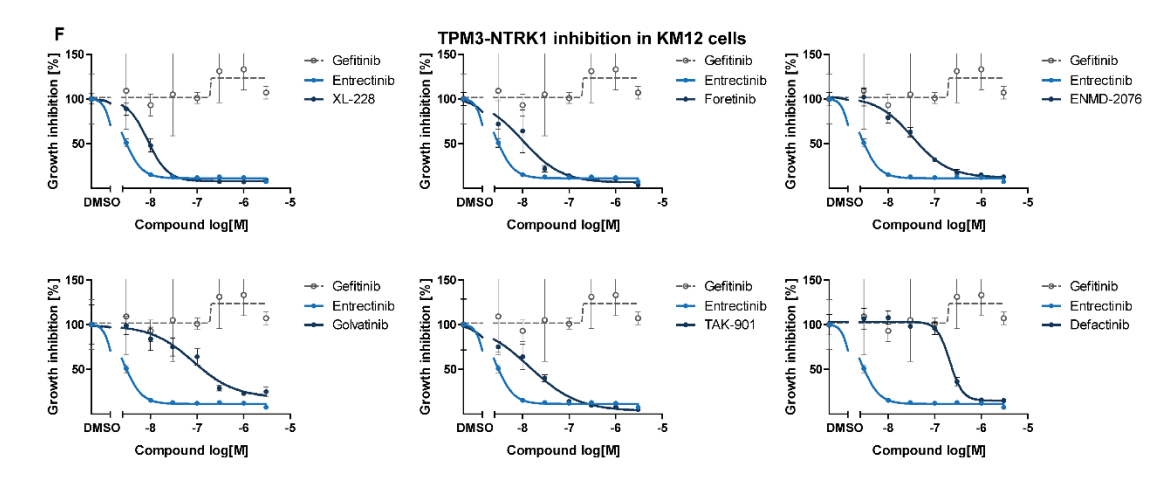


Fig. S6 continued | **Characterization of novel off-targets** – **NTRK1.** (**F**) Potential NTRK1 inhibitors but not Gefitinib reduced the viability of TPM3-NTRK1 dependent KM12 cells in a dose-dependent fashion (error bars show standard deviation of technical triplicates). The designated NTRK1 inhibitor Entrectinib was used as positive control.

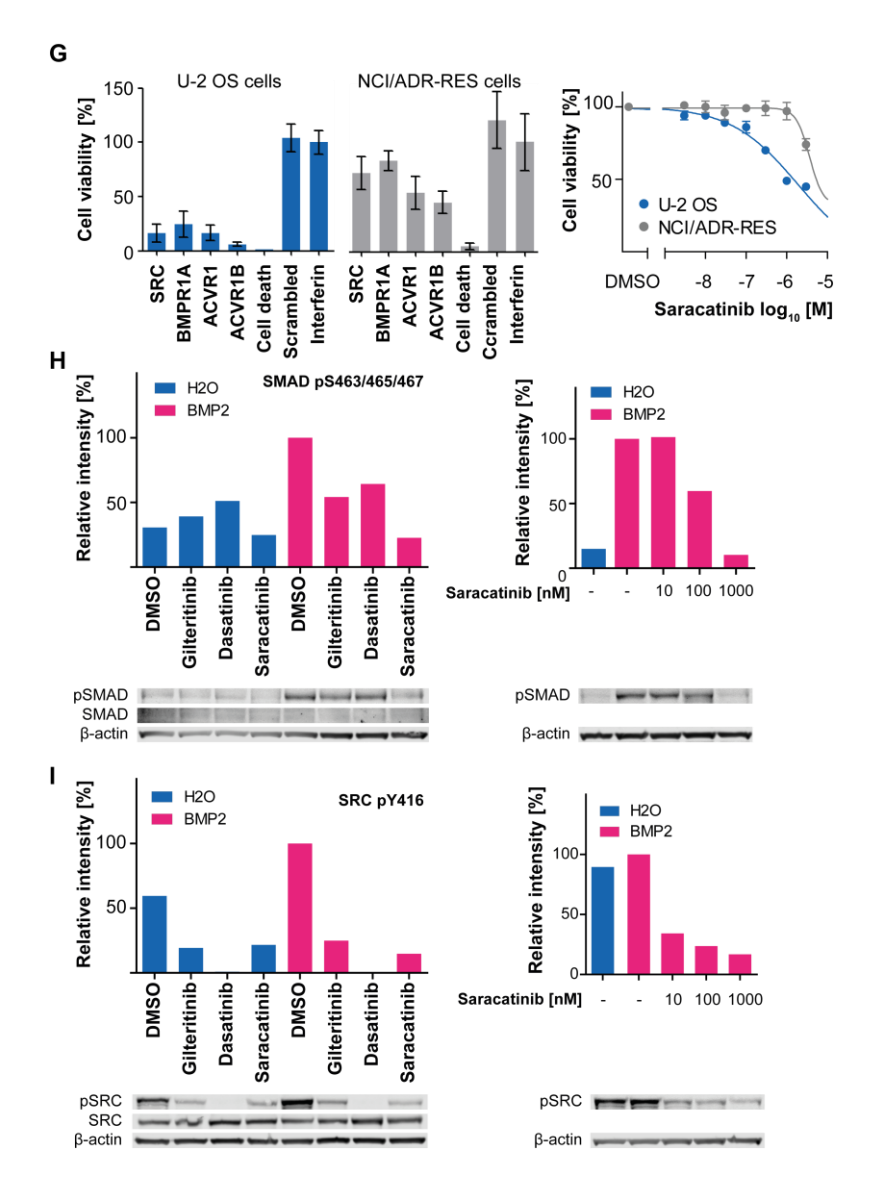


Fig. S6 continued | **Characterization of novel off-targets - Saracatinib.** (**G**) siRNA knock-down experiments in U-2 OS cells (osteosarcoma) and NCI/ADR-RES cells (ovarian cancer; left panel) suggested that Saracatinib efficacy in U-2 OS cells (right panel) is owing to a concerted inhibition of SRC and BMP receptor signaling in osteosarcoma. Transfection reagent and scrambled siRNAs were used as negative control and cell death inducing siRNA as positive control (error bars depict standard deviation of technical triplicates). (**H**) Western blot readout for phospho-SMAD in U-2 OS cells treated with inhibitor in the presence or absence of BMP2. Saracatinib treatment results in decreased phosphorylation of SMAD downstream of BMP receptors and (**I**) decreased autophosphorylation of SRC Y419 showing target/pathway engagement of the drug.

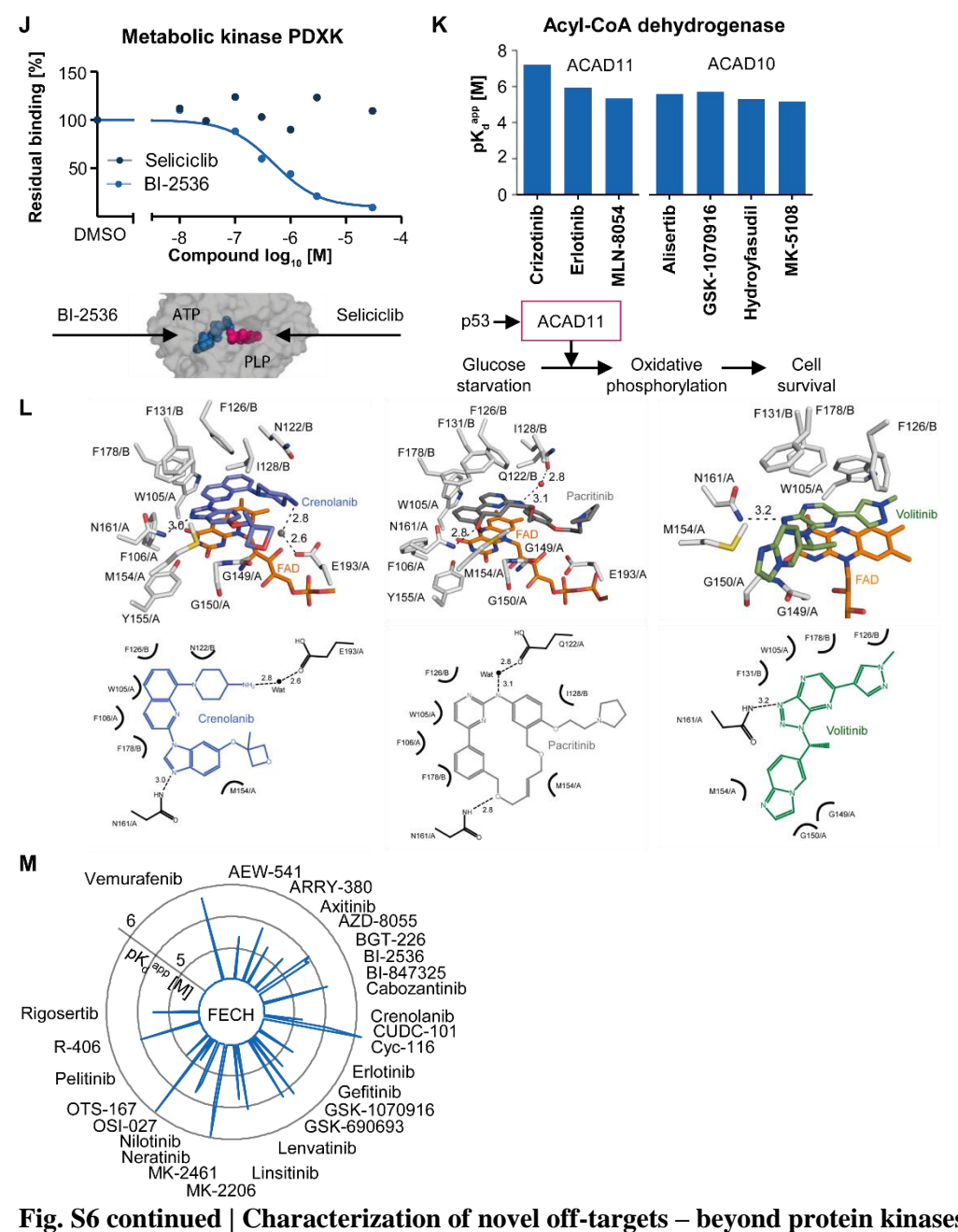


Fig. S6 continued | Characterization of novel off-targets – beyond protein kinases.

(J) Metabolic kinase PDXK as off-target of kinase inhibitors. Seliciclib is known to bind to the pyridoxal binding site (PLP) but does not score in the Kinobeads assay. Conversely, BI-2536 showed binding inhibition in Kinobeads and therefore likely interacts with the ATP-binding pocket of PDXK. (K) Acyl-CoA dehydrogenases ACAD10 and ACAD11 as off-targets of kinase inhibitors. Inhibition of ACAD11 may block the metabolic switch of cancer cells from glucose to fatty acid metabolism under conditions of glucose starvation. (L) Co-crystal structures of NQO2 and Crenolanib (left two panels), Pacritinib (middle two panels) and Volitinib (right two panels). All molecules interact with FAD by π -stacking and residues in the active site. (M) Radar plot of pK_d^{app} values for FECH revealing interaction with a total of 26 compounds.



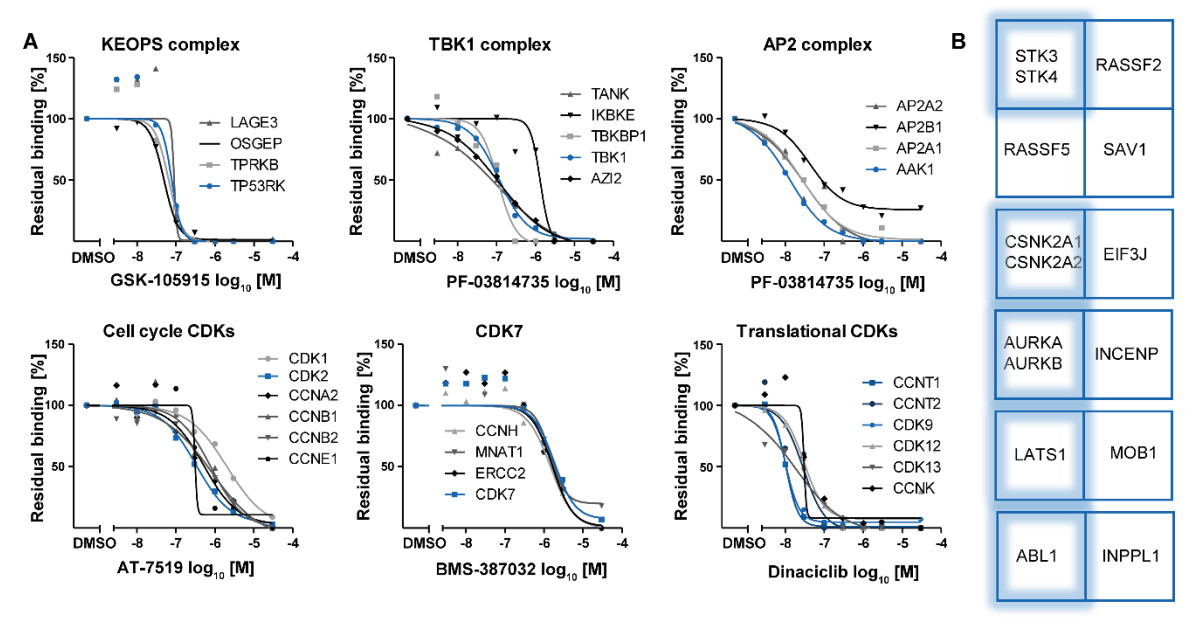


Fig. S7 | **Kinobeads binding of protein complexes** (**A**) Co-competed proteins forming KEOPS, TBK1, AP2 and CDK/Cyclin complexes are shown as examples. (**B**) Schematic representation of additional protein complexes identified in the Kinobeads pulldowns that showed similar curve characteristics (blue, direct Kinobead binder).

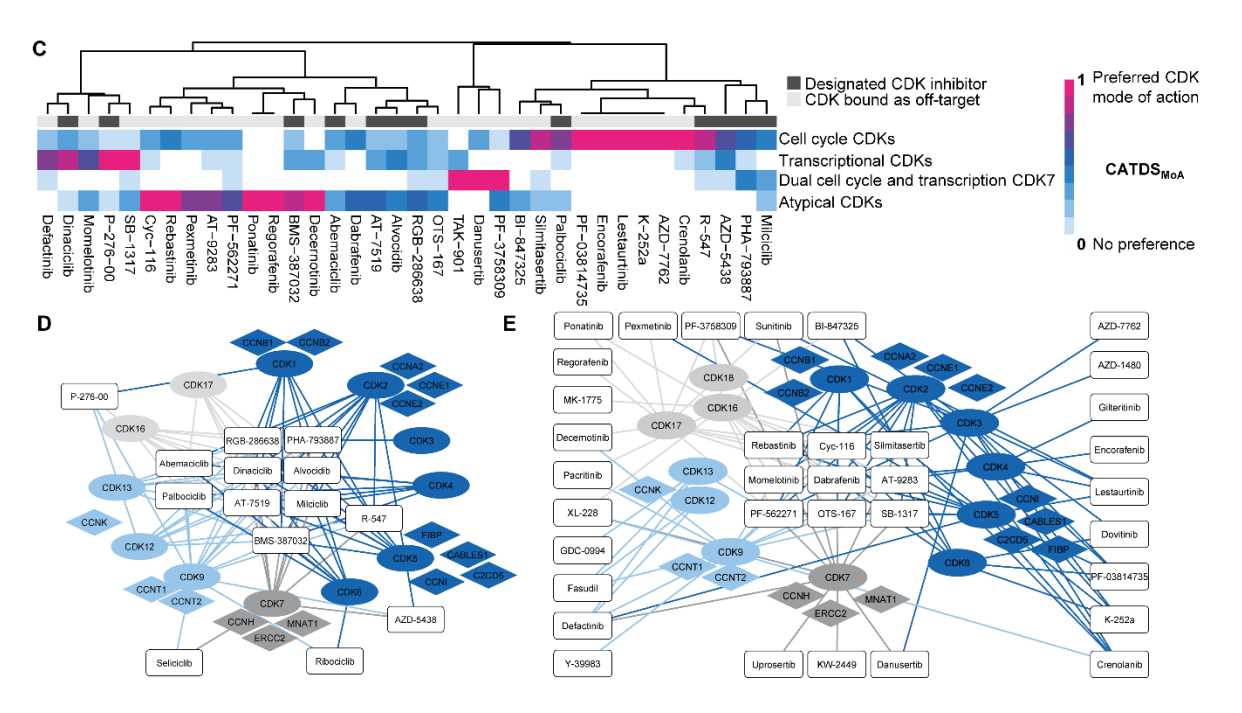


Fig. S7 continued | Kinobeads binding of protein complexes – CDKs. (C) Clustering of inhibitors targeting CDKs according to CATDS $_{MoA}$ (see Supplementary Materials for details). Compounds either had no preference (white-light blue) or targeted the same biological process (pink; e.g., the cell cycle). Off-target CDK inhibitors (light grey bar) often inhibited one potential CDK mode-of-action. (D) Designated CDK inhibitors targeted all CDK/cyclins irrespective of the biological process a particular complex is involved in (cell cycle in dark blue, translation in light blue, dual cell cycle and transcription CDK7 in dark grey, atypical CDKs in light grey). (E) Conversely, off-target CDK inhibitors showed some preference for the cell cycle (dark blue), translation (light blue), dual cell cycle and transcription CDK7 (dark grey) or atypical CDKs (light grey).

Fig. S8.

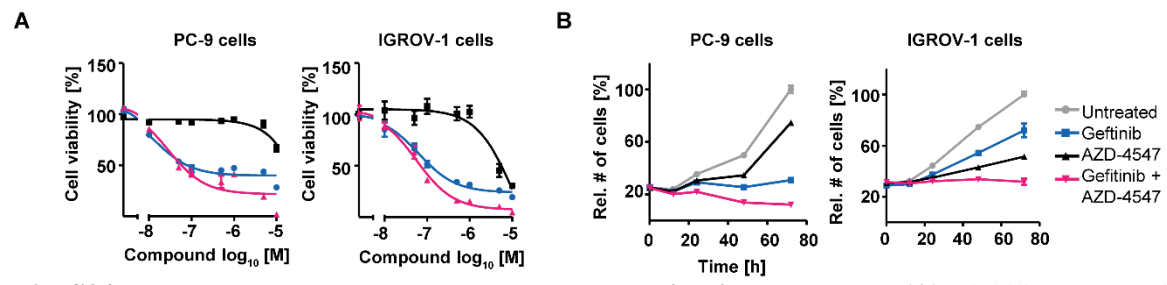


Fig. S8 | **From target to pathway engagement – combination treatment. (A)** Viability assays of drug combination treatment in lung (PC-9) and ovarian (IGROV-1) cancer cell lines. **(B)** Proliferation assays (from left to right) for PC-9 and IGROV-1 with single and drug combination treatment with Gefitinib and AZD-4547. Combination treatment of Gefitinib and AZD-4547 was more effective than any single drug. Experiments were performed in technical triplicates and error bars depict standard deviation.

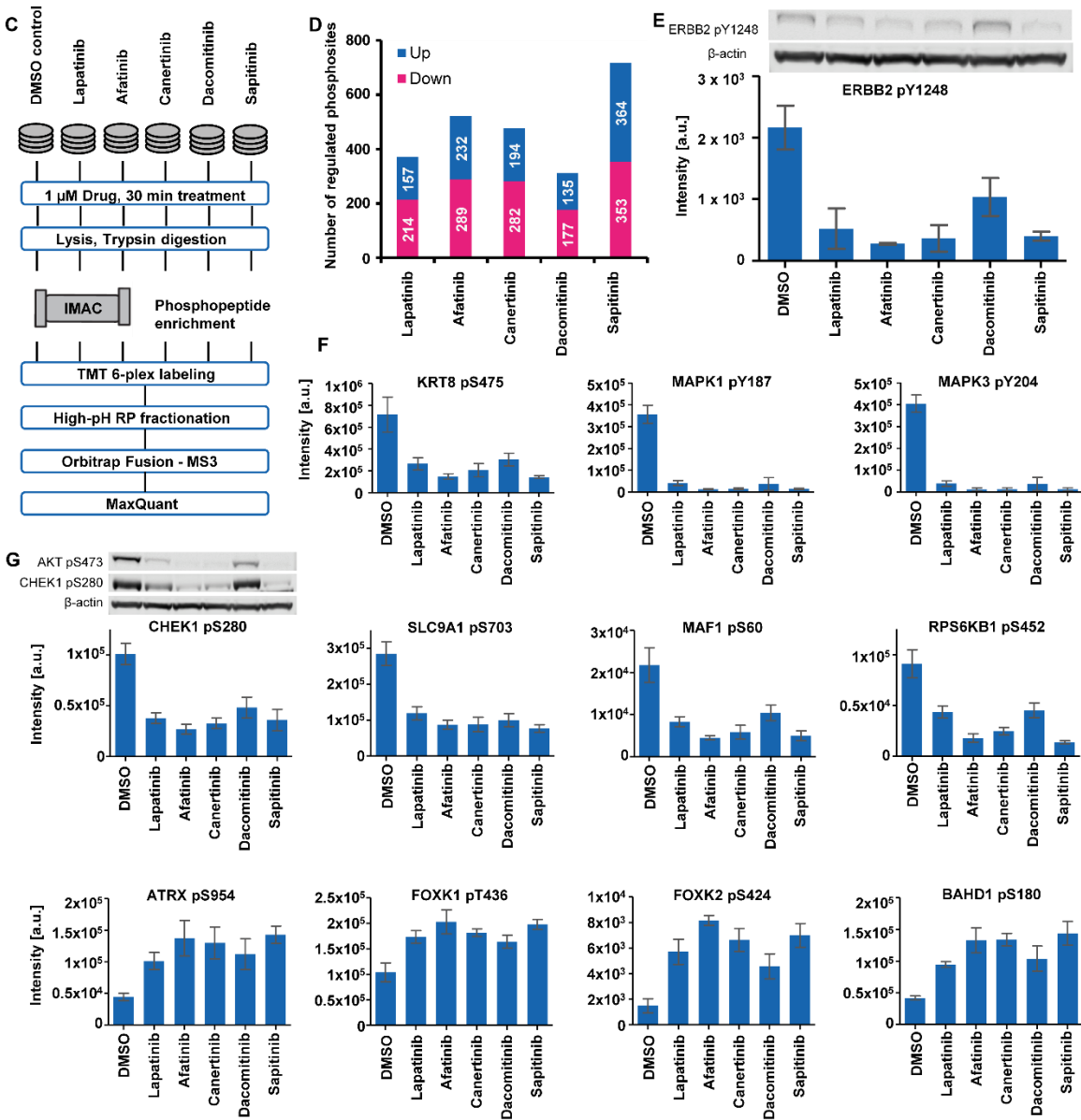


Fig. S8 continued | From target to pathway engagement – EGFR pathway. (C) Workflow for quantitative phosphoproteomics in BT-474 cell lines treated with different EGFR/ERBB2 inhibitors (in four replicates). (D) Number of reproducible (at least 3 from 4 biological replicates) significantly up- (blue) and down-regulated (pink) phosphorylated sites observed for each drug (two-sided t-test, p<0.01). (E) Down-regulation of the ERBB2 autophosphorylation site pY1248 can be used as a target engagement marker in cells for all drugs shown. (F-G) Up- and down-regulated phosphorylated sites for (F) known and (G) novel members of the ERBB2 network. Error bars depict the standard deviation. Further details are provided in the Supplementary Materials.

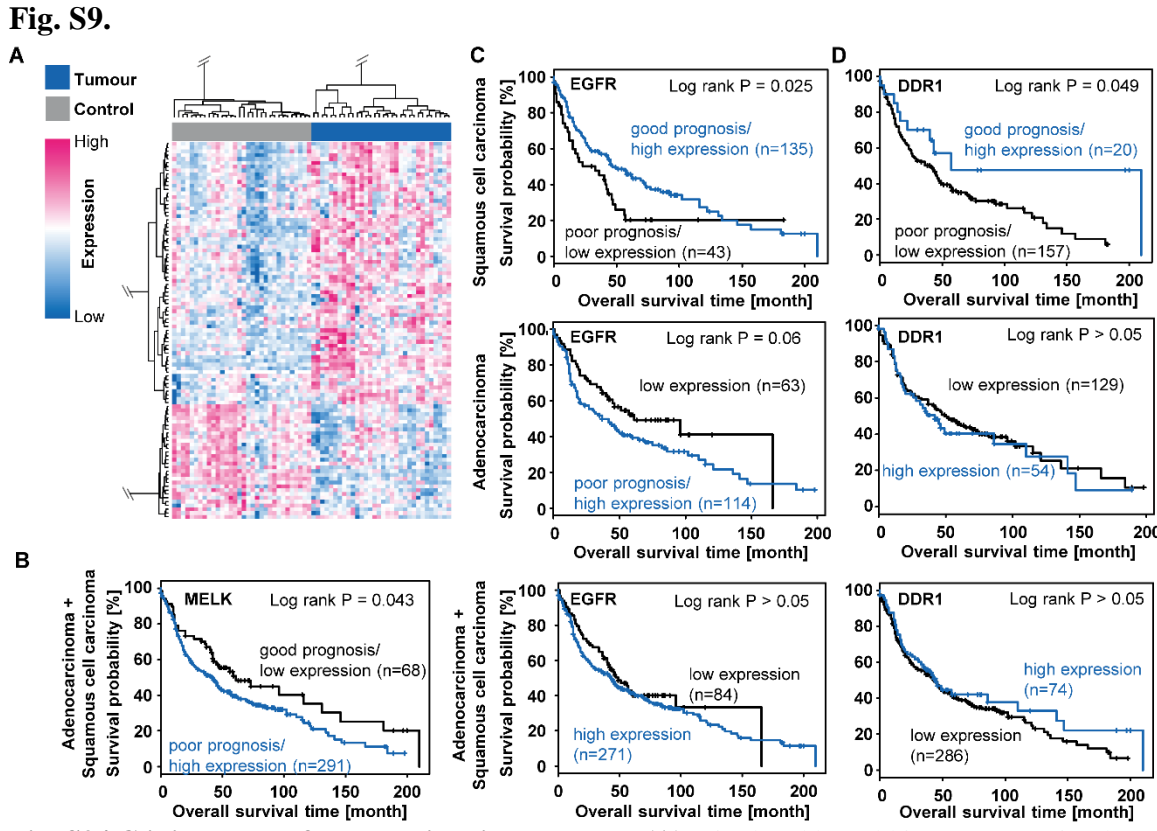


Fig. S9 | **Clinical drugs for potential kinase targets** (**A**) Kinobead based kinase expression heat map of healthy (grey) and tumour (blue) tissue from 15 NSCLC patients. Columns and rows are ordered according to the results from a supervised clustering (dendrogram) of significantly regulated kinases. (**B**) Combined Kaplan-Meier analysis of MELK in squamous cell carcinoma (SCC) and adenocarcinoma (ADC). (**C**) Kaplan-Meier analysis of EGFR in SCC, ADC and combined analysis. (**D**) Kaplan-Meier analysis of DDR1 in SCC, ADC and combined analysis. P-values were obtained from a log rank test.

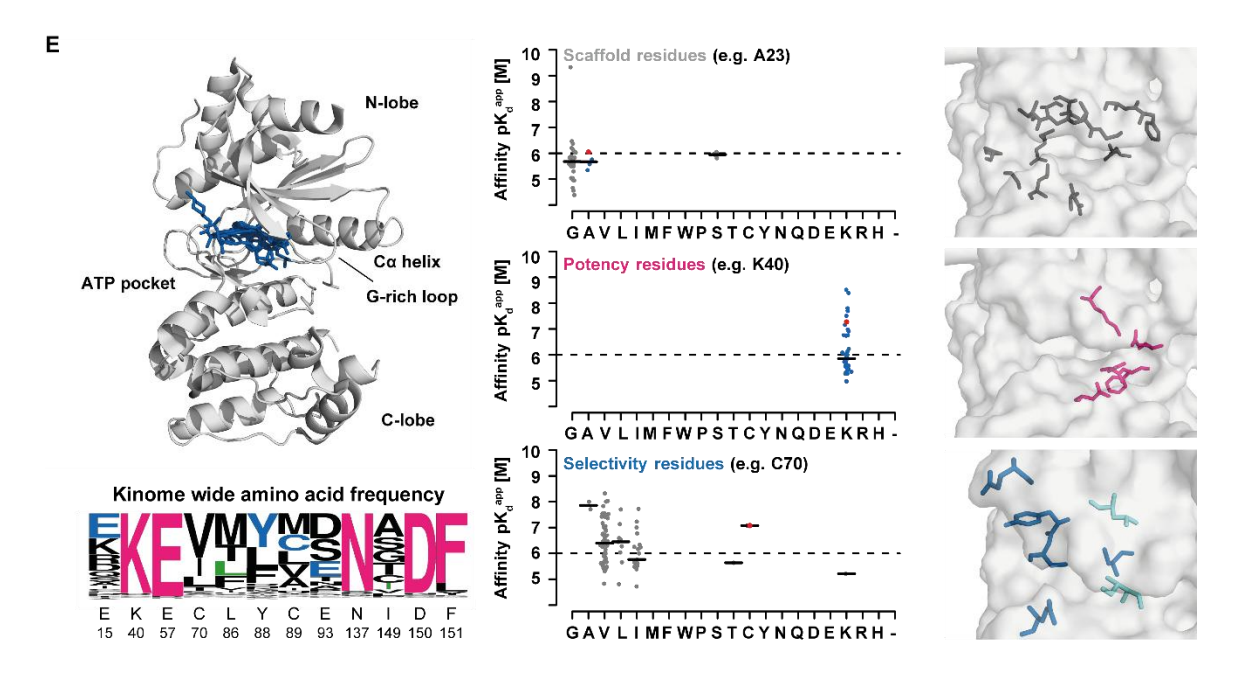


Fig. S9 continued | Clinical drugs for potential kinase targets (E) Co-crystal structures of MELK with Nintedanib, K-252a, PF-3758309, Defactinib and BI-847325 (left panel; superimposed compound structures in the ATP pocket in blue). The sequence logo shows kinome wide frequency of drug-interacting residues. Drug-interacting residues are classified as scaffold (grey), potency (pink) and selectivity (blue) residues (middle panel) and are localized within the ATP-pocket (right panel). A complete list of all residues plus classification is provided in Table S10 and Supplementary Materials.

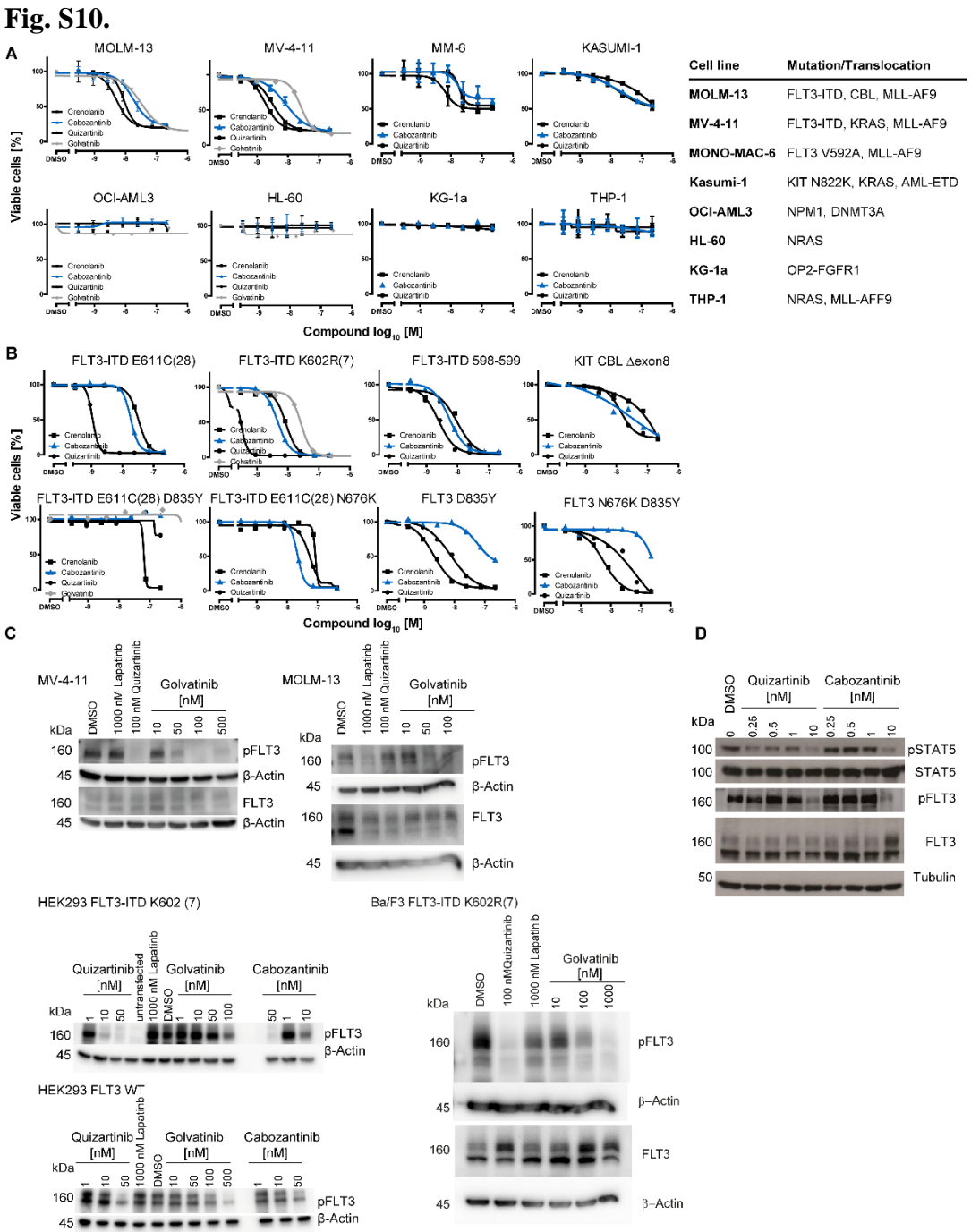


Fig. S10 | **Preclinical evaluation of Cabozantinib for treatment of AML.** (**A**) Cell viability assays for Cabozantinib, Golvatinib, Quizartinib and Crenolanib in AML cell lines (standard deviation of technical triplicates). Mutations and translocations of the cell lines are provided in the table (right). FLT3-mutated cell lines were sensitive towards FLT3 inhibition. (**B**) Proliferation assays for Cabozantinib, Golvatinib, Quizartinib and Crenolanib in Ba/F3 cells harbouring different FLT3 mutations. (**C**) Immunoblot analysis in MV-4-11 cells and MOLM-13, FLT3-WT and FLT3-ITD transfected HEK293 cells, and Ba/F3 FLT3-ITD cells revealed FLT3 target engagement for Golvatinib and Cabozantinib. FLT-ITD dependent cells are more sensitive to inhibitor treatment. (**D**) Immunoblot analysis of STAT5 phosphorylation for increasing doses of Quizartinib and Cabozantinib showed that both drugs can abrogate aberrant FLT3 signaling in MV-4-11 cells.

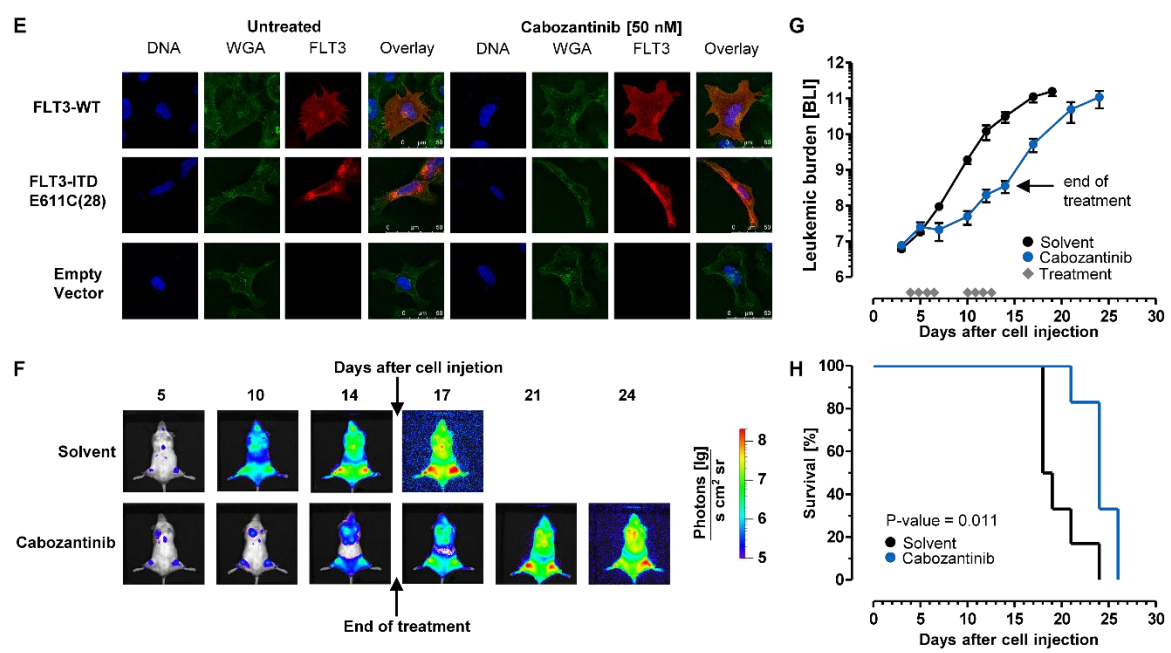


Fig. S10 continued | Preclinical evaluation of Cabozantinib for treatment of AML. (E) Immunofluorescence staining for FLT3-WT, FLT3-ITD 611C(28) or empty-vector transfected U-2 OS cells with no, or 6 h treatment with 50 nM Cabozantinib. Drug treatment restored membrane localization of FLT3-ITD analogous to WT. (**F-H**) NOD scid gamma mice were injected i.v. with MOLM13 cells. Three days post-injection, mice were treated with Cabozantinib (60 mg/kg) or left untreated. (**F**) Representative bioluminescence images of treated and control mice for up to 24 d after cell injection (MOLM-13). (**G**) BLI (bioluminescence in photons [lg]/(s*cm²*sr) signals for Cabozantinib- (blue, n=6) or vehicle-treated animals (black, n=5). Error bars depict standard deviation; diamonds indicate treatment days. (**H**) Kaplan-Meier survival curves for Cabozantinib (blue, n=6) or vehicle-treated animals (black, n=5). P-values were obtained after log rank test.

Table S1 (separate file)

Inhibitor annotation and MS experiment description

Table S2 (separate file)

Target Lists

Table S3 (separate file)

Drug Matrices

Table S4 (separate file)

Expression profiling

Table S5 (separate file)

Mutation Analysis

Table S6 (separate file)

Selectivities

Table S7 (separate file)

Literature Comparison

Table S8 (separate file)

SIK2 data

Table S9 (separate file)

Phosphorylation Dataset

Table S10 (separate file)

NSCLC

Table S11 (separate file)

MELK Structure

Table S12.Summary of kinase assay data performed at Reaction Biology Corporation. IC₅₀ values for kinases where obtained from dose responses in single measurements. Kinases not tested (n.d.) or not inhibited (n.i) are indicated as such.

Kinases	Dabrafenib IC50 [M]	Ponatinib IC50 [M]
ABL1	5.19E-06	< 1.00E-9
ABL2/ARG	2.94E-06	n.d.
ALK5/TGFBR1	9.87E-07	n.d.
ARAF	1.39E-10	n.d.
BRAF	6.30E-10	n.d.
BRAF (V599E)	4.05E-09	n.d.
BRK	1.13E-08	n.d.
CDK16/cyclin Y (PCTAIRE)	2.90E-08	n.d.
CDK1/cyclin A	5.69E-06	n.d.
CDK1/cyclin B	2.22E-06	n.d.
CDK1/cyclin E	2.92E-07	n.d.
CDK2/cyclin A	7.47E-06	n.d.
CDK2/cyclin A1	n.i.	n.d.
CDK2/cyclin E	n.i.	n.d.
CDK2/cyclin O	9.40E-06	n.d.
CDK3/cyclin E	6.86E-06	n.d.
CDK4/cyclin D1	8.52E-07	n.d.
CDK4/cyclin D3	1.84E-06	n.d.
CDK5/p25	4.92E-06	n.d.
CDK5/p35	3.71E-06	n.d.
CDK6/cyclin D1	n.i.	n.d.
CDK6/cyclin D3	5.37E-07	n.d.
CK1a1	n.i.	n.d.
CSK	4.24E-08	n.d.
EIF2AK1	4.82E-08	n.d.
FGR	5.35E-07	n.d.
FRK/PTK5	3.97E-07	n.d.
FYN	1.30E-06	n.d.
HPK1/MAP4K1	n.d.	3.62E-09
IRAK1	3.39E-06	4.02E-08
IRAK4	n.d.	5.32E-06
JNK2	n.d.	2.99E-06
LCK	4.50E-08	n.d.
LIMKI	3.22E-08	n.d. n.d.
LIMK2 LYN	3.59E-09 8.57E-08	n.d.
MEKKI	n.d.	1.36E-06
MLK3/MAP3K11	2.48E-06	n.d.
NEKI	9.58E-07	n.d.
NEKI NEKII	2.47E-08	n.d.
NEKII NEK9	4.70E-10	n.d.
p38a/MAPK14	n.d.	2.07E-08
PKCnu/PRKD3	8.40E-09	n.d.
PKD2/PRKD2	1.23E-07	n.d.
PLK4/SAK	3.47E-08	n.d.
RAF1	5.12E-10	n.d.
RIPK2	4.13E-08	
RIPK3	4.08E-09	
SIK2	4.23E-08	
SIK3	1.38E-07	
TAOK3/JIK		9.10E-06
TNK1	3.78E-08	-
ULK1	2.40E-07	
ZAK/MLTK	1.22E-08	< 1.00E-9

Table S13.Data collection and refinement statistics for drug-NQO2 co-crystals (molecular replacement). Data analysis and structure validation was carried out with MOLPROBITY(121) and PHENIX(122).

	NQO2	NQO2	NQO2
	Crenolanib	Pacritinib	Volitinib
	(5LBY)	(5LBZ)	(5LBW)
Data collection			
Space group	P212121	P212121	P212121
Cell dimensions			
$a, b, c (\mathring{A})$	61.6, 79.4, 106.6	61.4, 79.2, 106.2	57.4, 81.4, 106.4
α, β, γ (°)	90, 90, 90	90, 90, 90	90, 90, 90
Resolution (Å)	44.3 - 1.4	48.6 - 1.4	44.5 - 1.9
	(1.45 - 1.4)a	(1.45 - 1.4)a	(1.97-1.9)a
R_{merge}	0.039 (0.276)a	0.045 (0.329)a	0.110 (0.976)a
I/s(I)	22.6 (5.1)a	21.1 (5.3)a	7.5 (1.3)a
CC1/2	0.999 (0.95)a	0.999 (0.93)a	0.996 (0.56)a
Completeness (%)	0.93 (0.90)a	0.95 (0.91)a	0.90 (0.93)a
Redundancy	4.6 (64.4)a	4.5 (4.4)a	4.7 (4.0)a
Refinement			
Resolution (Å)	44.3 - 1.4	48.6 - 1.4	44.5 - 1.90
No. reflections	96,392	97,697	36,195
Rwork / Rfree	0.124 / 0.142	0.126 / 0.145	0.238/ 0.247
No. atoms			
Protein	3711	3697	3643
Ligands	174	198	160
Water	436	428	39
B factors			
Protein	14.6	13.1	42.1
Ligands	12.1	14.6	46.6
Water	26.9	25.1	37.7
R.m.s. deviations			
Bond lengths (Å)	0.96	0.96	0.97
Bond angles (°)	6.7	6.6	6.6
a Values in parantheses	are for highest resolution	ahall	

^a Values in parentheses are for highest-resolution shell.

Table S14.Data collection and refinement statistics for drug-MELK cocrystals (molecular replacement).

replacement).					
	MELK	MELK	MELK	MELK	MELK
	Nintedanib	PF-3758309	K-252a	Defactinib	<i>BI-847325</i>
	(5MAF)	(5MAG)	(5M5A)	(5MAH)	(5MAI)
Data collection					
Space group	P2 ₁ 2 ₁ 2 ₁	$P2_12_12_1$	$P2_12_12_1$	$P2_12_12_1$	$I4_{1}32$
Cell dimensions \square \square					
a, b, c (Å)	59.91, 63.71,	61.18, 62.81,	63.28, 91.21,	59.67, 63.70,	169.13,
	91.29	94.11	59.65	90.94	169.13, 169.13
α, β, γ (°)	90, 90, 90	90, 90, 90	90, 90, 90	90, 90, 90	90, 90, 90
Resolution (Å)	52.25 - 2.80	94.11 - 2.35	49.93 - 1.90	43.55 - 2.00	53.48 - 2.15
	(2.95 - 2.80) ^a	$(2.48 - 2.35)^a$	$(2.00 - 1.90)^a$	$(2.11 - 2.00)^a$	$(2.27 - 2.15)^a$
R_{merge}	0.129 (0.733) ^a	0.131 (0.369) ^a	0.032 (0.224) ^a	0.068 (0.735) ^a	0.063 (0.793) ^a
$I/\sigma(I)$	10.5 (2.6) ^a	$7.7 (3.9)^a$	21.3 (5.6) ^a	15.4 (2.5) ^a	18.1 (3.1) ^a
$CC_{1/2}$	0.993 (0.774) ^a	0.981 (0.885) ^a	1.000 (0.974) ^a	0.999 (0.824) ^a	0.999 (0.798) ^a
Completeness (%)	99.8 (99.8) ^a	95.9 (99.9) ^a	94.7 (84.2) ^a	98.3 (98.6) ^a	100.0 (100.0) ^a
Redundancy	6.0 (6.2) ^a	4.6 (4.8) ^a	4.5 (4.6) ^a	5.1 (4.9) ^a	8.6 (8.5) ^a
Refinement					
Resolution (Å)	52.25 - 2.80	52.24 - 2.35	49.93 - 1.90	43.55 - 2.00	53.49 - 2.15
No. reflections	8550	14303	19461	22356	21616
R_{work}/R_{free}	0.223 / 0.257	0.194 / 0.251	0.185 / 0.214	18.3 / 23.8	19.2 / 23.7
No. atoms					
Protein	2578	2586	2587	2604	2563
Ligand	40	35	35	35	35
Water	34	92	109	105	69
B factors					
Protein	57.01	36.42	43.85	38.46	54.60
Ligand	51.42	32.19	36.74	35.66	65.12
Water	46.57	35.72	47.23	42.52	55.01
R.m.s. deviations					
Bond lengths (Å)	0.0076	0.0091	0.0116	0.0107	0.0120
Bond angles (°)	1.2854	1.4091	1.8555	1.4383	1.5352
		1 - 41 1 11			

^a Values in parentheses are for highest-resolution shell.

Table S15.Clinical pathology parameters of the human NSCLC tissue samples.

		Total	Adenocarcinoma	Squamous cell carcinoma
Number of pati	ents [n]	375	186	189
Gender [%]				
	Female	25	37	14
	Male	75	63	86
Age [years]				
	Average	65	63	66
	Range	31-83	31-83	43-82
pT category [%	6]			
	pT1	23	32	14
	pT2	49	46	52
	pT3	19	15	24
	pT4	8	7	10
Lymph node m	netastasis [%]			
	pN0	57	58	56
	pN1	15	10	20
	pN2	26	28	23
	pN3	1	2	1
	pNX	1	2	1
Distant metast	asis [%]			
	MO	97	95	99
	M1	3	5	1
Residual tumo	ur [%]			
	R0	89	90	88
	R1	9	10	7
	R2	1	0	1
	RX	2	0	4

 $\label{eq:total_continuous_series} \textbf{Table S16.}$ Panel of AML cell lines with mutation information and sensitivity data for Cabozantinib, Crenolanib, and Quizartinib measured by an MTS-assay. Number in brackets gives EC for Cabozantinib in the respective cell line.

Cell line	Described mutations	FLT3 inhibitor sensitivity	FLT3 expression
THP-1	NRAS, MLL-AF9	no	yes
OCI-AML3	NPM1, DNMT3A	no	yes
OCI-AML5		no	yes
U-937		no	no
KG-1a	OP1-FGFR1	no	no
NB-4	PML-RARA	no	no
HL-60	NRAS	no	no
SD-1	BCR-ABL	no	no
K-562	BCR-ABL	no	no
MV-4-11	FLT3-ITD (homozygous), MLL-AF9	yes (16 nM)	yes
MOLM-13	FLT3-ITD (heterozygous), MLL-AF9	yes (73 nM)	yes
MONO-MAC-1	FLT3 V592A, MLL-AF9	yes (34 nM)	yes
MONO-MAC-6	FLT3 V592A, MLL-AF9	yes (288 nM)	yes
EOL-1	FIP1L1-PDGFRA	yes (1 nM)	yes
KASUMI-1	KIT N822K, KRAS, AML-ETO	yes (69 nM)	no

Table S17.Cell viability data (EC₅₀ in nM) for kinase inhibitors in AML cell lines and stable Ba/F3 cell lines expressing different FLT3 constructs (n.i. means no inhibition).

Cell line	Cabozantinib	Quizartinib	Crenolanib	Golvatinib
MOLM-13	18	5	8	32
MV-4-11	8	2	3	26
MONO-MAC-6	16	7	19	
Kasumi-1	19	17	>100	
OCI-AML3	n.i.	n.i.	n.i.	n.i.
HL-60	n.i.	n.i.	n.i.	n.i.
KG-1a	n.i.	n.i.	n.i.	
THP-1	n.i.	n.i.	n.i.	
FLT3-ITD E611C(28)	18	1	33	
FLT3-ITD K602R(7)	5	0.3	9	
FLT3-ITD 598/599(22)	5	2	10	
KIT CBL $\Delta exon8$	32	14	>100	
FLT3-ITD E611C(28) D835Y	n.i.	n.i.	64	
FLT3-ITD E611C(28) N676K	22	58	85	
FLT3 D835Y	57	7	2	
FLT3 N676K D835Y	>100	66	6	

FLT3-ITD Nomenclature according to Janke et al.(85) and Arreba-Tutusaus et al.(123):

FLT3-ITD K602R(7) = FLT3-ITD (w51) = FLT3-ITD 3

FLT3-ITD E611C(28) = FLT3-ITD (Npos) = FLT3-ITD 2

FLT3-ITD 598/599(22) = FLT3-ITD (w78) = FLT3-ITD 1

References

- 1. P. Wu, T. E. Nielsen, M. H. Clausen, FDA-approved small-molecule kinase inhibitors. *Trends Pharmacol. Sci.* **36**, 422–439 (2015). doi: <u>10.1016/j.tips.2015.04.005</u>; <u>Medline</u>
- 2. D. Fabbro, S. W. Cowan-Jacob, H. Moebitz, Ten things you should know about protein kinases: IUPHAR review 14. *Br. J. Pharmacol.* **172**, 2675–2700 (2015). doi: 10.1111/bph.13096; Medline
- 3. M. W. Karaman, S. Herrgard, D. K. Treiber, P. Gallant, C. E. Atteridge, B. T. Campbell, K. W. Chan, P. Ciceri, M. I. Davis, P. T. Edeen, R. Faraoni, M. Floyd, J. P. Hunt, D. J. Lockhart, Z. V. Milanov, M. J. Morrison, G. Pallares, H. K. Patel, S. Pritchard, L. M. Wodicka, P. P. Zarrinkar, A quantitative analysis of kinase inhibitor selectivity. *Nat. Biotechnol.* **26**, 127–132 (2008). doi: 10.1038/nbt1358; Medline
- 4. Y. Gao, S. P. Davies, M. Augustin, A. Woodward, U. A. Patel, R. Kovelman, K. J. Harvey, A broad activity screen in support of a chemogenomic map for kinase signalling research and drug discovery. *Biochem. J.* **451**, 313–328 (2013). doi: <u>10.1042/BJ20121418</u>; <u>Medline</u>
- 5. M. I. Davis, J. P. Hunt, S. Herrgard, P. Ciceri, L. M. Wodicka, G. Pallares, M. Hocker, D. K. Treiber, P. P. Zarrinkar, Comprehensive analysis of kinase inhibitor selectivity. *Nat. Biotechnol.* **29**, 1046–1051 (2011). doi: 10.1038/nbt.1990; Medline
- 6. T. Anastassiadis, S. W. Deacon, K. Devarajan, H. Ma, J. R. Peterson, Comprehensive assay of kinase catalytic activity reveals features of kinase inhibitor selectivity. *Nat. Biotechnol.* **29**, 1039–1045 (2011). doi: 10.1038/nbt.2017; Medline
- 7. J. Bain, L. Plater, M. Elliott, N. Shpiro, C. J. Hastie, H. Mclauchlan, I. Klevernic, J. S. C. Arthur, D. R. Alessi, P. Cohen, The selectivity of protein kinase inhibitors: A further update. *Biochem. J.* **408**, 297–315 (2007). doi: 10.1042/BJ20070797; Medline
- 8. M. A. Fabian, W. H. Biggs III, D. K. Treiber, C. E. Atteridge, M. D. Azimioara, M. G. Benedetti, T. A. Carter, P. Ciceri, P. T. Edeen, M. Floyd, J. M. Ford, M. Galvin, J. L. Gerlach, R. M. Grotzfeld, S. Herrgard, D. E. Insko, M. A. Insko, A. G. Lai, J.-M. Lélias, S. A. Mehta, Z. V. Milanov, A. M. Velasco, L. M. Wodicka, H. K. Patel, P. P. Zarrinkar, D. J. Lockhart, A

- small molecule–kinase interaction map for clinical kinase inhibitors. *Nat. Biotechnol.* **23**, 329–336 (2005). doi: 10.1038/nbt1068; Medline
- 9. S. P. Davies, H. Reddy, M. Caivano, P. Cohen, Specificity and mechanism of action of some commonly used protein kinase inhibitors. *Biochem. J.* **351**, 95–105 (2000). doi: 10.1042/bj3510095; Medline
- 10. J. M. Elkins, V. Fedele, M. Szklarz, K. R. Abdul Azeez, E. Salah, J. Mikolajczyk, S. Romanov, N. Sepetov, X.-P. Huang, B. L. Roth, A. Al Haj Zen, D. Fourches, E. Muratov, A. Tropsha, J. Morris, B. A. Teicher, M. Kunkel, E. Polley, K. E. Lackey, F. L. Atkinson, J. P. Overington, P. Bamborough, S. Müller, D. J. Price, T. M. Willson, D. H. Drewry, S. Knapp, W. J. Zuercher, Comprehensive characterization of the Published Kinase Inhibitor Set. *Nat. Biotechnol.* 34, 95–103 (2016). doi: 10.1038/nbt.3374; Medline
- 11. J. T. Metz, E. F. Johnson, N. B. Soni, P. J. Merta, L. Kifle, P. J. Hajduk, Navigating the kinome. *Nat. Chem. Biol.* **7**, 200–202 (2011). doi: 10.1038/nchembio.530; Medline
- 12. HMS LINCS Database, http://lincs.hms.harvard.edu/db/ (2016).
- 13. M. Bantscheff, D. Eberhard, Y. Abraham, S. Bastuck, M. Boesche, S. Hobson, T. Mathieson, J. Perrin, M. Raida, C. Rau, V. Reader, G. Sweetman, A. Bauer, T. Bouwmeester, C. Hopf, U. Kruse, G. Neubauer, N. Ramsden, J. Rick, B. Kuster, G. Drewes, Quantitative chemical proteomics reveals mechanisms of action of clinical ABL kinase inhibitors. *Nat. Biotechnol.* 25, 1035–1044 (2007). doi: 10.1038/nbt1328; Medline
- 14. G. Médard, F. Pachl, B. Ruprecht, S. Klaeger, S. Heinzlmeir, D. Helm, H. Qiao, X. Ku, M. Wilhelm, T. Kuehne, Z. Wu, A. Dittmann, C. Hopf, K. Kramer, B. Kuster, Optimized chemical proteomics assay for kinase inhibitor profiling. *J. Proteome Res.* **14**, 1574–1586 (2015). doi: 10.1021/pr5012608; Medline
- 15. M. Wilhelm, J. Schlegl, H. Hahne, A. M. Gholami, M. Lieberenz, M. M. Savitski, E. Ziegler, L. Butzmann, S. Gessulat, H. Marx, T. Mathieson, S. Lemeer, K. Schnatbaum, U. Reimer, H. Wenschuh, M. Mollenhauer, J. Slotta-Huspenina, J.-H. Boese, M. Bantscheff, A. Gerstmair, F. Faerber, B. Kuster, Mass-spectrometry-based draft of the human proteome. *Nature* **509**, 582–587 (2014). doi: 10.1038/nature13319; Medline

- 16. M. P. Patricelli, T. K. Nomanbhoy, J. Wu, H. Brown, D. Zhou, J. Zhang, S. Jagannathan, A. Aban, E. Okerberg, C. Herring, B. Nordin, H. Weissig, Q. Yang, J. D. Lee, N. S. Gray, J. W. Kozarich, In situ kinase profiling reveals functionally relevant properties of native kinases. *Chem. Biol.* **18**, 699–710 (2011). doi: 10.1016/j.chembiol.2011.04.011; Medline
- 17. J. J. Sutherland, C. Gao, S. Cahya, M. Vieth, What general conclusions can we draw from kinase profiling data sets? *Biochim. Biophys. Acta* **1834**, 1425–1433 (2013). doi: 10.1016/j.bbapap.2012.12.023; Medline
- 18. A. F. Rudolf, T. Skovgaard, S. Knapp, L. J. Jensen, J. Berthelsen, A comparison of protein kinases inhibitor screening methods using both enzymatic activity and binding affinity determination. *PLOS ONE* **9**, e98800 (2014). doi: 10.1371/journal.pone.0098800; Medline
- 19. P. P. Graczyk, Gini coefficient: A new way to express selectivity of kinase inhibitors against a family of kinases. *J. Med. Chem.* **50**, 5773–5779 (2007). doi: 10.1021/jm070562u; Medline
- 20. J. C. M. Uitdehaag, G. J. R. Zaman, A theoretical entropy score as a single value to express inhibitor selectivity. *BMC Bioinformatics* **12**, 94 (2011). doi: <u>10.1186/1471-2105-12-94</u>; <u>Medline</u>
- 21. A. C. Cheng, J. Eksterowicz, S. Geuns-Meyer, Y. Sun, Analysis of kinase inhibitor selectivity using a thermodynamics-based partition index. *J. Med. Chem.* **53**, 4502–4510 (2010). doi: 10.1021/jm100301x; Medline
- 22. S. Knapp, P. Arruda, J. Blagg, S. Burley, D. H. Drewry, A. Edwards, D. Fabbro, P. Gillespie, N. S. Gray, B. Kuster, K. E. Lackey, P. Mazzafera, N. C. O. Tomkinson, T. M. Willson, P. Workman, W. J. Zuercher, A public-private partnership to unlock the untargeted kinome. *Nat. Chem. Biol.* **9**, 3–6 (2013). doi: 10.1038/nchembio.1113; Medline
- 23. A. J. Kooistra, G. K. Kanev, O. P. J. van Linden, R. Leurs, I. J. P. de Esch, C. de Graaf, KLIFS: A structural kinase-ligand interaction database. *Nucleic Acids Res.* **44**, D365–D371 (2016). doi: 10.1093/nar/gkv1082; Medline
- 24. Z. Zhao, H. Wu, L. Wang, Y. Liu, S. Knapp, Q. Liu, N. S. Gray, Exploration of type II binding mode: A privileged approach for kinase inhibitor focused drug discovery? *ACS Chem. Biol.* **9**, 1230–1241 (2014). doi: 10.1021/cb500129t; Medline

- 25 J. F. Ohren, H. Chen, A. Pavlovsky, C. Whitehead, E. Zhang, P. Kuffa, C. Yan, P. McConnell, C. Spessard, C. Banotai, W. T. Mueller, A. Delaney, C. Omer, J. Sebolt-Leopold, D. T. Dudley, I. K. Leung, C. Flamme, J. Warmus, M. Kaufman, S. Barrett, H. Tecle, C. A. Hasemann, Structures of human MAP kinase kinase 1 (MEK1) and MEK2 describe novel noncompetitive kinase inhibition. *Nat. Struct. Mol. Biol.* 11, 1192–1197 (2004). doi: 10.1038/nsmb859; Medline
- 26. A. P. Bento, A. Gaulton, A. Hersey, L. J. Bellis, J. Chambers, M. Davies, F. A. Krüger, Y. Light, L. Mak, S. McGlinchey, M. Nowotka, G. Papadatos, R. Santos, J. P. Overington, The ChEMBL bioactivity database: An update. *Nucleic Acids Res.* **42**, D1083–D1090 (2014). doi: 10.1093/nar/gkt1031; Medline
- 27. A. Fauster, M. Rebsamen, K. V. M. Huber, J. W. Bigenzahn, A. Stukalov, C.-H. Lardeau, S. Scorzoni, M. Bruckner, M. Gridling, K. Parapatics, J. Colinge, K. L. Bennett, S. Kubicek, S. Krautwald, A. Linkermann, G. Superti-Furga, A cellular screen identifies ponatinib and pazopanib as inhibitors of necroptosis. *Cell Death Dis.* **6**, e1767 (2015). doi: 10.1038/cddis.2015.130; Medline
- 28. K. Clark, K. F. MacKenzie, K. Petkevicius, Y. Kristariyanto, J. Zhang, H. G. Choi, M. Peggie, L. Plater, P. G. A. Pedrioli, E. McIver, N. S. Gray, J. S. C. Arthur, P. Cohen, Phosphorylation of CRTC3 by the salt-inducible kinases controls the interconversion of classically activated and regulatory macrophages. *Proc. Natl. Acad. Sci. U.S.A.* **109**, 16986–16991 (2012). doi: 10.1073/pnas.1215450109; Medline
- 29. J. Ozanne, A. R. Prescott, K. Clark, The clinically approved drugs dasatinib and bosutinib induce anti-inflammatory macrophages by inhibiting the salt-inducible kinases. *Biochem. J.* **465**, 271–279 (2015). doi: 10.1042/BJ20141165; Medline
- 30. T. S. Gujral, L. Peshkin, M. W. Kirschner, Exploiting polypharmacology for drug target deconvolution. *Proc. Natl. Acad. Sci. U.S.A.* **111**, 5048–5053 (2014). doi: 10.1073/pnas.1403080111; Medline
- 31. A. C. Peterson, J. D. Russell, D. J. Bailey, M. S. Westphall, J. J. Coon, Parallel reaction monitoring for high resolution and high mass accuracy quantitative, targeted proteomics. *Mol. Cell. Proteomics* **11**, 1475–1488 (2012). doi: 10.1074/mcp.O112.020131; Medline

- 32. S. Gallien, E. Duriez, C. Crone, M. Kellmann, T. Moehring, B. Domon, Targeted proteomic quantification on quadrupole-orbitrap mass spectrometer. *Mol. Cell. Proteomics* **11**, 1709–1723 (2012). doi: 10.1074/mcp.O112.019802; Medline
- 33. E. Ardini, R. Bosotti, A. L. Borgia, C. De Ponti, A. Somaschini, R. Cammarota, N. Amboldi, L. Raddrizzani, A. Milani, P. Magnaghi, D. Ballinari, D. Casero, F. Gasparri, P. Banfi, N. Avanzi, M. B. Saccardo, R. Alzani, T. Bandiera, E. Felder, D. Donati, E. Pesenti, A. Sartore-Bianchi, M. Gambacorta, M. A. Pierotti, S. Siena, S. Veronese, A. Galvani, A. Isacchi, The TPM3-NTRK1 rearrangement is a recurring event in colorectal carcinoma and is associated with tumor sensitivity to TRKA kinase inhibition. *Mol. Oncol.* **8**, 1495–1507 (2014). doi: 10.1016/j.molonc.2014.06.001; Medline
- 34. A. Vaishnavi, M. Capelletti, A. T. Le, S. Kako, M. Butaney, D. Ercan, S. Mahale, K. D. Davies, D. L. Aisner, A. B. Pilling, E. M. Berge, J. Kim, H. Sasaki, S.-i. Park, G. Kryukov, L. A. Garraway, P. S. Hammerman, J. Haas, S. W. Andrews, D. Lipson, P. J. Stephens, V. A. Miller, M. Varella-Garcia, P. A. Jänne, R. C. Doebele, Oncogenic and drug-sensitive *NTRK1* rearrangements in lung cancer. *Nat. Med.* **19**, 1469–1472 (2013). doi: 10.1038/nm.3352; Medline
- 35. P. J. Cook, R. Thomas, R. Kannan, E. S. de Leon, A. Drilon, M. K. Rosenblum, M. Scaltriti, R. Benezra, A. Ventura, Somatic chromosomal engineering identifies BCAN-NTRK1 as a potent glioma driver and therapeutic target. *Nat. Commun.* **8**, 15987 (2017). doi: 10.1038/ncomms15987; Medline
- 36. L. Tang, M.-H. Li, P. Cao, F. Wang, W.-R. Chang, S. Bach, J. Reinhardt, Y. Ferandin, H. Galons, Y. Wan, N. Gray, L. Meijer, T. Jiang, D.-C. Liang, Crystal structure of pyridoxal kinase in complex with roscovitine and derivatives. *J. Biol. Chem.* **280**, 31220–31229 (2005). doi: 10.1074/jbc.M500805200; Medline
- 37. J. A. Winger, O. Hantschel, G. Superti-Furga, J. Kuriyan, The structure of the leukemia drug imatinib bound to human quinone reductase 2 (NQO2). *BMC Struct. Biol.* **9**, 7 (2009). doi: 10.1186/1472-6807-9-7; Medline
- 38. S. Klaeger, B. Gohlke, J. Perrin, V. Gupta, S. Heinzlmeir, D. Helm, H. Qiao, G. Bergamini, H. Handa, M. M. Savitski, M. Bantscheff, G. Médard, R. Preissner, B. Kuster,

- Chemical proteomics reveals ferrochelatase as a common off-target of kinase inhibitors. *ACS Chem. Biol.* **11**, 1245–1254 (2016). doi: 10.1021/acschembio.5b01063; Medline
- 39. M. M. Savitski, F. B. M. Reinhard, H. Franken, T. Werner, M. F. Savitski, D. Eberhard, D. Martinez Molina, R. Jafari, R. B. Dovega, S. Klaeger, B. Kuster, P. Nordlund, M. Bantscheff, G. Drewes, Tracking cancer drugs in living cells by thermal profiling of the proteome. *Science* **346**, 1255784 (2014). doi: 10.1126/science.1255784; Medline
- 40. C. Borgo, C. Franchin, V. Salizzato, L. Cesaro, G. Arrigoni, L. Matricardi, L. A. Pinna, A. Donella-Deana, Protein kinase CK2 potentiates translation efficiency by phosphorylating eIF3j at Ser127. *Biochim. Biophys. Acta* **1853**, 1693–1701 (2015). doi: 10.1016/j.bbamcr.2015.04.004; Medline
- 41. H. Koch, M. Wilhelm, B. Ruprecht, S. Beck, M. Frejno, S. Klaeger, B. Kuster, Phosphoproteome profiling reveals molecular mechanisms of growth-factor-mediated kinase inhibitor resistance in EGFR-overexpressing cancer cells. *J. Proteome Res.* **15**, 4490–4504 (2016). doi: 10.1021/acs.jproteome.6b00621; Medline
- 42. P. Mertins, D. R. Mani, K. V. Ruggles, M. A. Gillette, K. R. Clauser, P. Wang, X. Wang, J. W. Qiao, S. Cao, F. Petralia, E. Kawaler, F. Mundt, K. Krug, Z. Tu, J. T. Lei, M. L. Gatza, M. Wilkerson, C. M. Perou, V. Yellapantula, K.-l. Huang, C. Lin, M. D. McLellan, P. Yan, S. R. Davies, R. R. Townsend, S. J. Skates, J. Wang, B. Zhang, C. R. Kinsinger, M. Mesri, H. Rodriguez, L. Ding, A. G. Paulovich, D. Fenyö, M. J. Ellis, S. A. Carr; NCI CPTAC, Proteogenomics connects somatic mutations to signalling in breast cancer. *Nature* **534**, 55–62 (2016). doi: 10.1038/nature18003; Medline
- 43. Y. Li, H. Tang, Z. Sun, A. O. Bungum, E. S. Edell, W. L. Lingle, S. M. Stoddard, M. Zhang, J. Jen, P. Yang, L. Wang, Network-based approach identified cell cycle genes as predictor of overall survival in lung adenocarcinoma patients. *Lung Cancer* **80**, 91–98 (2013). doi: 10.1016/j.lungcan.2012.12.022; Medline
- 44. A. Lin, C. J. Giuliano, N. M. Sayles, J. M. Sheltzer, CRISPR/Cas9 mutagenesis invalidates a putative cancer dependency targeted in on-going clinical trials. *eLife* **6**, e24179 (2017). doi: 10.7554/eLife.24179; Medline

- 45. H.-T. Huang, H.-S. Seo, T. Zhang, Y. Wang, B. Jiang, Q. Li, D. L. Buckley, B. Nabet, J. M. Roberts, J. Paulk, S. Dastjerdi, G. E. Winter, H. McLauchlan, J. Moran, J. E. Bradner, M. J. Eck, S. Dhe-Paganon, J. J. Zhao, N. S. Gray, MELK is not necessary for the proliferation of basal-like breast cancer cells. *eLife* 6, e26693 (2017). doi: 10.7554/eLife.26693; Medline
- 46. S. Heinzlmeir, D. Kudlinzki, S. Sreeramulu, S. Klaeger, S. L. Gande, V. Linhard, M. Wilhelm, H. Qiao, D. Helm, B. Ruprecht, K. Saxena, G. Médard, H. Schwalbe, B. Kuster, Chemical proteomics and structural biology define EPHA2 inhibition by clinical kinase drugs. *ACS Chem. Biol.* **11**, 3400–3411 (2016). doi: 10.1021/acschembio.6b00709; Medline
- 47. E. Buchdunger, C. L. Cioffi, N. Law, D. Stover, S. Ohno-Jones, B. J. Druker, N. B. Lydon, Abl protein-tyrosine kinase inhibitor STI571 inhibits in vitro signal transduction mediated by c-kit and platelet-derived growth factor receptors. *J. Pharmacol. Exp. Ther.* **295**, 139–145 (2000). Medline
- 48. F. M. Yakes, J. Chen, J. Tan, K. Yamaguchi, Y. Shi, P. Yu, F. Qian, F. Chu, F. Bentzien, B. Cancilla, J. Orf, A. You, A. D. Laird, S. Engst, L. Lee, J. Lesch, Y.-C. Chou, A. H. Joly, Cabozantinib (XL184), a novel MET and VEGFR2 inhibitor, simultaneously suppresses metastasis, angiogenesis, and tumor growth. *Mol. Cancer Ther.* **10**, 2298–2308 (2011). doi: 10.1158/1535-7163.MCT-11-0264; Medline
- 49. C. Choudhary, J. V. Olsen, C. Brandts, J. Cox, P. N. G. Reddy, F. D. Böhmer, V. Gerke, D.-E. Schmidt-Arras, W. E. Berdel, C. Müller-Tidow, M. Mann, H. Serve, Mislocalized activation of oncogenic RTKs switches downstream signaling outcomes. *Mol. Cell* **36**, 326–339 (2009). doi: 10.1016/j.molcel.2009.09.019; Medline
- 50. J.-W. Lu, A.-N. Wang, H.-A. Liao, C.-Y. Chen, H.-A. Hou, C.-Y. Hu, H.-F. Tien, D.-L. Ou, L.-I. Lin, Cabozantinib is selectively cytotoxic in acute myeloid leukemia cells with *FLT3*-internal tandem duplication (FLT3-ITD). *Cancer Lett.* **376**, 218–225 (2016). doi: 10.1016/j.canlet.2016.04.004; Medline
- 51. H. Hahne, F. Pachl, B. Ruprecht, S. K. Maier, S. Klaeger, D. Helm, G. Médard, M. Wilm, S. Lemeer, B. Kuster, DMSO enhances electrospray response, boosting sensitivity of proteomic experiments. *Nat. Methods* **10**, 989–991 (2013). doi: 10.1038/nmeth.2610; Medline

- 52. J. Cox, M. Mann, MaxQuant enables high peptide identification rates, individualized p.p.b.-range mass accuracies and proteome-wide protein quantification. *Nat. Biotechnol.* **26**, 1367–1372 (2008). doi: 10.1038/nbt.1511; Medline
- 53. J. Cox, N. Neuhauser, A. Michalski, R. A. Scheltema, J. V. Olsen, M. Mann, Andromeda: A peptide search engine integrated into the MaxQuant environment. *J. Proteome Res.* **10**, 1794–1805 (2011). doi: 10.1021/pr101065j; Medline
- 54. J. Cox, M. Y. Hein, C. A. Luber, I. Paron, N. Nagaraj, M. Mann, Accurate proteome-wide label-free quantification by delayed normalization and maximal peptide ratio extraction, termed MaxLFQ. *Mol. Cell. Proteomics* **13**, 2513–2526 (2014). doi: 10.1074/mcp.M113.031591; Medline
- 55. C. Ritz, F. Baty, J. C. Streibig, D. Gerhard, Dose-response analysis using R. *PLOS ONE* **10**, e0146021 (2015). doi: 10.1371/journal.pone.0146021; Medline
- 56. S. Lemeer, C. Zörgiebel, B. Ruprecht, K. Kohl, B. Kuster, Comparing immobilized kinase inhibitors and covalent ATP probes for proteomic profiling of kinase expression and drug selectivity. *J. Proteome Res.* **12**, 1723–1731 (2013). doi: 10.1021/pr301073j; Medline
- 57. H. Thorvaldsdóttir, J. T. Robinson, J. P. Mesirov, Integrative Genomics Viewer (IGV): High-performance genomics data visualization and exploration. *Brief. Bioinform.* **14**, 178–192 (2013). doi: 10.1093/bib/bbs017; Medline
- 58. J. T. Robinson, H. Thorvaldsdóttir, W. Winckler, M. Guttman, E. S. Lander, G. Getz, J. P. Mesirov, Integrative genomics viewer. *Nat. Biotechnol.* **29**, 24–26 (2011). doi: 10.1038/nbt.1754; Medline
- 59. B. Ruprecht, H. Koch, G. Medard, M. Mundt, B. Kuster, S. Lemeer, Comprehensive and reproducible phosphopeptide enrichment using iron immobilized metal ion affinity chromatography (Fe-IMAC) columns. *Mol. Cell. Proteomics* **14**, 205–215 (2015). doi: 10.1074/mcp.M114.043109; Medline
- 60. J. Rappsilber, M. Mann, Y. Ishihama, Protocol for micro-purification, enrichment, pre-fractionation and storage of peptides for proteomics using StageTips. *Nat. Protoc.* **2**, 1896–1906 (2007). doi: 10.1038/nprot.2007.261; Medline

- 61. B. MacLean, D. M. Tomazela, N. Shulman, M. Chambers, G. L. Finney, B. Frewen, R. Kern, D. L. Tabb, D. C. Liebler, M. J. MacCoss, Skyline: An open source document editor for creating and analyzing targeted proteomics experiments. *Bioinformatics* **26**, 966–968 (2010). doi: 10.1093/bioinformatics/btq054; Medline
- 62. A. M. Gholami, H. Hahne, Z. Wu, F. J. Auer, C. Meng, M. Wilhelm, B. Kuster, Global proteome analysis of the NCI-60 cell line panel. *Cell Rep.* **4**, 609–620 (2013). doi: 10.1016/j.celrep.2013.07.018; Medline
- 63. W. Kabsch, Integration, scaling, space-group assignment and post-refinement. *Acta Crystallogr. D Biol. Crystallogr.* **66**, 133–144 (2010). doi: <u>10.1107/S0907444909047374</u>; <u>Medline</u>
- 64. W. Kabsch, XDS. *Acta Crystallogr. D Biol. Crystallogr.* **66**, 125–132 (2010). doi: 10.1107/S0907444909047337; Medline
- 65. K. Diederichs, P. A. Karplus, Better models by discarding data? *Acta Crystallogr. D Biol. Crystallogr.* **69**, 1215–1222 (2013). doi: 10.1107/S0907444913001121; Medline
- 66. P. Evans, Resolving some old problems in protein crystallography. *Science* **336**, 986–987 (2012). doi: <u>10.1126/science.1222162</u>; <u>Medline</u>
- 67. P. A. Karplus, K. Diederichs, Linking crystallographic model and data quality. *Science* **336**, 1030–1033 (2012). doi: 10.1126/science.1218231; Medline
- 68. M. D. Winn, C. C. Ballard, K. D. Cowtan, E. J. Dodson, P. Emsley, P. R. Evans, R. M. Keegan, E. B. Krissinel, A. G. W. Leslie, A. McCoy, S. J. McNicholas, G. N. Murshudov, N. S. Pannu, E. A. Potterton, H. R. Powell, R. J. Read, A. Vagin, K. S. Wilson, Overview of the *CCP*4 suite and current developments. *Acta Crystallogr. D Biol. Crystallogr.* 67, 235–242 (2011). doi: 10.1107/S0907444910045749; Medline
- 69. G. N. Murshudov, A. A. Vagin, E. J. Dodson, Refinement of macromolecular structures by the maximum-likelihood method. *Acta Crystallogr. D Biol. Crystallogr.* **53**, 240–255 (1997). doi: 10.1107/S0907444996012255; Medline
- 70. G. N. Murshudov, P. Skubák, A. A. Lebedev, N. S. Pannu, R. A. Steiner, R. A. Nicholls, M. D. Winn, F. Long, A. A. Vagin, *REFMAC*5 for the refinement of macromolecular crystal

- structures. *Acta Crystallogr. D Biol. Crystallogr.* **67**, 355–367 (2011). doi: 10.1107/S0907444911001314; Medline
- 71. P. Emsley, B. Lohkamp, W. G. Scott, K. Cowtan, Features and development of *Coot. Acta Crystallogr. D Biol. Crystallogr.* **66**, 486–501 (2010). doi: 10.1107/S0907444910007493; Medline
- 72. E. Krissinel, K. Henrick, Secondary-structure matching (SSM), a new tool for fast protein structure alignment in three dimensions. *Acta Crystallogr. D Biol. Crystallogr.* **60**, 2256–2268 (2004). doi: 10.1107/S0907444904026460; Medline
- 73. A. C. Wallace, R. A. Laskowski, J. M. Thornton, LIGPLOT: A program to generate schematic diagrams of protein-ligand interactions. *Protein Eng.* **8**, 127–134 (1995). doi: 10.1093/protein/8.2.127; Medline
- 74. G. Canevari, S. Re Depaolini, U. Cucchi, J. A. Bertrand, E. Casale, C. Perrera, B. Forte, P. Carpinelli, E. R. Felder, Structural insight into maternal embryonic leucine zipper kinase (MELK) conformation and inhibition toward structure-based drug design. *Biochemistry* **52**, 6380–6387 (2013). doi: 10.1021/bi4005864; Medline
- 75. T. G. G. Battye, L. Kontogiannis, O. Johnson, H. R. Powell, A. G. W. Leslie, *iMOSFLM*: A new graphical interface for diffraction-image processing with *MOSFLM*. *Acta Crystallogr*. *D Biol. Crystallogr*. **67**, 271–281 (2011). doi: 10.1107/S0907444910048675; Medline
- 76. P. Evans, Scaling and assessment of data quality. *Acta Crystallogr. D Biol. Crystallogr.* **62**, 72–82 (2006). doi: <u>10.1107/S0907444905036693</u>; <u>Medline</u>
- 77. A. J. McCoy, R. W. Grosse-Kunstleve, P. D. Adams, M. D. Winn, L. C. Storoni, R. J. Read, *Phaser* crystallographic software. *J. Appl. Crystallogr.* **40**, 658–674 (2007). doi: 10.1107/S0021889807021206; Medline
- 78. J. R. Wiśniewski, A. Zougman, N. Nagaraj, M. Mann, Universal sample preparation method for proteome analysis. *Nat. Methods* **6**, 359–362 (2009). doi: <u>10.1038/nmeth.1322</u>; <u>Medline</u>

- 79. S. Tyanova, T. Temu, P. Sinitcyn, A. Carlson, M. Y. Hein, T. Geiger, M. Mann, J. Cox, The Perseus computational platform for comprehensive analysis of (prote)omics data. *Nat. Methods* **13**, 731–740 (2016). doi: 10.1038/nmeth.3901; Medline
- 80. D. Szklarczyk, A. Franceschini, S. Wyder, K. Forslund, D. Heller, J. Huerta-Cepas, M. Simonovic, A. Roth, A. Santos, K. P. Tsafou, M. Kuhn, P. Bork, L. J. Jensen, C. von Mering, STRING v10: Protein–protein interaction networks, integrated over the tree of life. *Nucleic Acids Res.* **43**, D447–D452 (2015). doi: 10.1093/nar/gku1003; Medline
- 81. Z. Wu, A. M. Gholami, B. Kuster, Systematic identification of the HSP90 candidate regulated proteome. *Mol. Cell. Proteomics* **11**, M111.016675 (2012). doi: 10.1074/mcp.M111.016675; Medline
- 82. V. Ermolayev, P. Mohajerani, A. Ale, A. Sarantopoulos, M. Aichler, G. Kayser, A. Walch, V. Ntziachristos, Early recognition of lung cancer by integrin targeted imaging in K-ras mouse model. *Int. J. Cancer* **137**, 1107–1118 (2015). doi: 10.1002/ijc.29372; Medline
- 83. G. Kayser, A. Csanadi, C. Otto, T. Plönes, N. Bittermann, J. Rawluk, B. Passlick, M. Werner, Simultaneous multi-antibody staining in non-small cell lung cancer strengthens diagnostic accuracy especially in small tissue samples. *PLOS ONE* **8**, e56333 (2013). doi: 10.1371/journal.pone.0056333; Medline
- 84. H. Polzer, H. Janke, D. Schmid, W. Hiddemann, K. Spiekermann, Casitas B-lineage lymphoma mutants activate AKT to induce transformation in cooperation with class III receptor tyrosine kinases. *Exp. Hematol.* **41**, 271–280 (2013). doi: 10.1016/j.exphem.2012.10.016; Medline
- 85. H. Janke, F. Pastore, D. Schumacher, T. Herold, K.-P. Hopfner, S. Schneider, W. E. Berdel, T. Büchner, B. J. Woermann, M. Subklewe, S. K. Bohlander, W. Hiddemann, K. Spiekermann, H. Polzer, Activating FLT3 mutants show distinct gain-of-function phenotypes in vitro and a characteristic signaling pathway profile associated with prognosis in acute myeloid leukemia. *PLOS ONE* **9**, e89560 (2014). doi: 10.1371/journal.pone.0089560; Medline
- 86. H. Polzer, H. Janke, S. Schneider, W. Hiddemann, M. Subklewe, K. Spiekermann, Individualized treatment strategy with small-molecular inhibitors in acute myeloid leukemia

- with concurrent FLT3-ITD and FLT3-TKD mutation. *J. Clin. Case Rep.* **5**, 622 (2015). doi: 10.4172/2165-7920.1000622
- 87. B. A. Rabinovich, Y. Ye, T. Etto, J. Q. Chen, H. I. Levitsky, W. W. Overwijk, L. J. N. Cooper, J. Gelovani, P. Hwu, Visualizing fewer than 10 mouse T cells with an enhanced firefly luciferase in immunocompetent mouse models of cancer. *Proc. Natl. Acad. Sci. U.S.A.* **105**, 14342–14346 (2008). doi: 10.1073/pnas.0804105105; Medline
- 88. N. Terziyska, C. Castro Alves, V. Groiss, K. Schneider, K. Farkasova, M. Ogris, E. Wagner, H. Ehrhardt, R. J. Brentjens, U. zur Stadt, M. Horstmann, L. Quintanilla-Martinez, I. Jeremias, In vivo imaging enables high resolution preclinical trials on patients' leukemia cells growing in mice. *PLOS ONE* 7, e52798 (2012). doi: 10.1371/journal.pone.0052798; Medline
- 89. K. Sharma, C. Weber, M. Bairlein, Z. Greff, G. Kéri, J. Cox, J. V. Olsen, H. Daub, Proteomics strategy for quantitative protein interaction profiling in cell extracts. *Nat. Methods* **6**, 741–744 (2009). doi: 10.1038/nmeth.1373; Medline
- 90. J. C. M. Uitdehaag, F. Verkaar, H. Alwan, J. de Man, R. C. Buijsman, G. J. R. Zaman, A guide to picking the most selective kinase inhibitor tool compounds for pharmacological validation of drug targets. *Br. J. Pharmacol.* **166**, 858–876 (2012). doi: 10.1111/j.1476-5381.2012.01859.x; Medline
- 91. G. M. Simon, M. J. Niphakis, B. F. Cravatt, Determining target engagement in living systems. *Nat. Chem. Biol.* **9**, 200–205 (2013). doi: 10.1038/nchembio.1211; Medline
- 92. K. Clark, Protein kinase networks that limit TLR signalling. *Biochem. Soc. Trans.* **42**, 11–24 (2014). doi: <u>10.1042/BST20130124</u>; <u>Medline</u>
- 93. K. F. MacKenzie, K. Clark, S. Naqvi, V. A. McGuire, G. Nöehren, Y. Kristariyanto, M. van den Bosch, M. Mudaliar, P. C. McCarthy, M. J. Pattison, P. G. A. Pedrioli, G. J. Barton, R. Toth, A. Prescott, J. S. C. Arthur, PGE₂ induces macrophage IL-10 production and a regulatory-like phenotype via a protein kinase A–SIK–CRTC3 pathway. *J. Immunol.* **190**, 565–577 (2013). doi: 10.4049/jimmunol.1202462; Medline
- 94. T. B. Sundberg, H. G. Choi, J.-H. Song, C. N. Russell, M. M. Hussain, D. B. Graham, B. Khor, J. Gagnon, D. J. O'Connell, K. Narayan, V. Dančík, J. R. Perez, H.-C. Reinecker, N. S. Gray, S. L. Schreiber, R. J. Xavier, A. F. Shamji, Small-molecule screening identifies

- inhibition of salt-inducible kinases as a therapeutic strategy to enhance immunoregulatory functions of dendritic cells. *Proc. Natl. Acad. Sci. U.S.A.* **111**, 12468–12473 (2014). doi: 10.1073/pnas.1412308111; Medline
- 95. M. S. Lombardi, C. Gilliéron, D. Dietrich, C. Gabay, SIK inhibition in human myeloid cells modulates TLR and IL-1R signaling and induces an anti-inflammatory phenotype. *J. Leukoc. Biol.* **99**, 711–721 (2016). doi: 10.1189/jlb.2A0715-307R; Medline
- 96. S. Rocha, M. D. Garrett, K. J. Campbell, K. Schumm, N. D. Perkins, Regulation of NF-κB and p53 through activation of ATR and Chk1 by the ARF tumour suppressor. *EMBO J.* **24**, 1157–1169 (2005). doi: 10.1038/sj.emboj.7600608; Medline
- 97. K. J. Campbell, J. M. Witty, S. Rocha, N. D. Perkins, Cisplatin mimics ARF tumor suppressor regulation of RelA (p65) nuclear factor-κB transactivation. *Cancer Res.* **66**, 929–935 (2006). doi: 10.1158/0008-5472.CAN-05-2234; Medline
- 98. B. Chaurasia, J. Mauer, L. Koch, J. Goldau, A.-S. Kock, J. C. Brüning, Phosphoinositide-dependent kinase 1 provides negative feedback inhibition to Toll-like receptor-mediated NF-κB activation in macrophages. *Mol. Cell Biol.* **30**, 4354–4366 (2010). doi: 10.1128/MCB.00069-10; Medline
- 99. L. F. Hennequin, J. Allen, J. Breed, J. Curwen, M. Fennell, T. P. Green, C. Lambert-van der Brempt, R. Morgentin, R. A. Norman, A. Olivier, L. Otterbein, P. A. Plé, N. Warin, G. Costello, *N*-(5-chloro-1,3-benzodioxol-4-yl)-7-[2-(4-methylpiperazin-1-yl)ethoxy]-5- (tetrahydro-2*H*-pyran-4-yloxy)quinazolin-4-amine, a novel, highly selective, orally available, dual-specific c-Src/Abl kinase inhibitor. *J. Med. Chem.* **49**, 6465–6488 (2006). doi: 10.1021/jm060434q; Medline
- 100. A. C. Shor, E. A. Keschman, F. Y. Lee, C. Muro-Cacho, G. D. Letson, J. C. Trent, W. J. Pledger, R. Jove, Dasatinib inhibits migration and invasion in diverse human sarcoma cell lines and induces apoptosis in bone sarcoma cells dependent on Src kinase for survival. *Cancer Res.* **67**, 2800–2808 (2007). doi: 10.1158/0008-5472.CAN-06-3469; Medline
- 101. Q. Chen, Z. Zhou, L. Shan, H. Zeng, Y. Hua, Z. Cai, The importance of Src signaling in sarcoma. *Oncol. Lett.* **10**, 17–22 (2015). doi: 10.3892/ol.2015.3184; Medline

- 102. T. C. Lewis, R. Prywes, Serum regulation of Id1 expression by a BMP pathway and BMP responsive element. *Biochim. Biophys. Acta* **1829**, 1147–1159 (2013). doi: 10.1016/j.bbagrm.2013.08.002; Medline
- 103. A. Nguyen, M. A. Scott, S. M. Dry, A. W. James, Roles of bone morphogenetic protein signaling in osteosarcoma. *Int. Orthop.* **38**, 2313–2322 (2014). doi: 10.1007/s00264-014-2512-x; Medline
- 104. L. le Gallic, D. Sgouras, G. Beal Jr., G. Mavrothalassitis, Transcriptional repressor ERF is a Ras/mitogen-activated protein kinase target that regulates cellular proliferation. *Mol. Cell Biol.* **19**, 4121–4133 (1999). doi: 10.1128/MCB.19.6.412110330152; Medline
- 105. L. Le Gallic, L. Virgilio, P. Cohen, B. Biteau, G. Mavrothalassitis, ERF nuclear shuttling, a continuous monitor of Erk activity that links it to cell cycle progression. *Mol. Cell Biol.* **24**, 1206–1218 (2004). doi: 10.1128/MCB.24.3.1206-1218.2004; Medline
- 106. A. E. Lagarde, A. J. Franchi, S. Paris, J. M. Pouysségur, Effect of mutations affecting Na⁺: H⁺ antiport activity on tumorigenic potential of hamster lung fibroblasts. *J. Cell. Biochem.* **36**, 249–260 (1988). doi: 10.1002/jcb.240360306; Medline
- 107. L. Shan, X. Zhou, X. Liu, Y. Wang, D. Su, Y. Hou, N. Yu, C. Yang, B. Liu, J. Gao, Y. Duan, J. Yang, W. Li, J. Liang, L. Sun, K. Chen, C. Xuan, L. Shi, Y. Wang, Y. Shang, FOXK2 elicits massive transcription repression and suppresses the hypoxic response and breast cancer carcinogenesis. *Cancer Cell* **30**, 708–722 (2016). doi: 10.1016/j.ccell.2016.09.010; Medline
- 108. R. A. Cardone, V. Casavola, S. J. Reshkin, The role of disturbed pH dynamics and the Na⁺/H⁺ exchanger in metastasis. *Nat. Rev. Cancer* **5**, 786–795 (2005). doi: 10.1038/nrc1713; Medline
- 109. H. Bierne, T. N. Tham, E. Batsche, A. Dumay, M. Leguillou, S. Kernéis-Golsteyn, B. Regnault, J. S. Seeler, C. Muchardt, J. Feunteun, P. Cossart, Human BAHD1 promotes heterochromatic gene silencing. *Proc. Natl. Acad. Sci. U.S.A.* **106**, 13826–13831 (2009). doi: 10.1073/pnas.0901259106; Medline

- 110. S. A. Stuart, S. Houel, T. Lee, N. Wang, W. M. Old, N. G. Ahn, A phosphoproteomic comparison of B-RAF^{V600E} and MKK1/2 inhibitors in melanoma cells. *Mol. Cell. Proteomics* **14**, 1599–1615 (2015). doi: 10.1074/mcp.M114.047233; Medline
- 111. L. Galluzzi, I. Vitale, L. Senovilla, K. A. Olaussen, G. Pinna, T. Eisenberg, A. Goubar, I. Martins, J. Michels, G. Kratassiouk, D. Carmona-Gutierrez, M. Scoazec, E. Vacchelli, F. Schlemmer, O. Kepp, S. Shen, M. Tailler, M. Niso-Santano, E. Morselli, A. Criollo, S. Adjemian, M. Jemaà, K. Chaba, C. Pailleret, M. Michaud, F. Pietrocola, N. Tajeddine, T. de La Motte Rouge, N. Araujo, N. Morozova, T. Robert, H. Ripoche, F. Commo, B. Besse, P. Validire, P. Fouret, A. Robin, N. Dorvault, P. Girard, S. Gouy, P. Pautier, N. Jägemann, A. C. Nickel, S. Marsili, C. Paccard, N. Servant, P. Hupé, C. Behrens, P. Behnam-Motlagh, K. Kohno, I. Cremer, D. Damotte, M. Alifano, Ø Midttun, P. M. Ueland, V. Lazar, P. Dessen, H. Zischka, E. Chatelut, M. Castedo, F. Madeo, E. Barillot, J. Thomale, I. I. Wistuba, C. Sautès-Fridman, L. Zitvogel, J. C. Soria, A. Harel-Bellan, G. Kroemer, Prognostic impact of vitamin B6 metabolism in lung cancer. *Cell Rep.* 2, 257–269 (2012). doi: 10.1016/j.celrep.2012.06.017; Medline
- 112. D. Jiang, E. L. LaGory, D. Kenzelmann Brož, K. T. Bieging, C. A. Brady, N. Link, J. M. Abrams, A. J. Giaccia, L. D. Attardi, Analysis of p53 transactivation domain mutants reveals *Acad11* as a metabolic target important for p53 pro-survival function. *Cell Rep.* **10**, 1096–1109 (2015). doi: 10.1016/j.celrep.2015.01.043; Medline
- 113. E. A. Meyer, R. K. Castellano, F. Diederich, Interactions with aromatic rings in chemical and biological recognition. *Angew. Chem. Int. Ed. Engl.* **42**, 1210–1250 (2003). doi: 10.1002/anie.200390319; Medline
- 114. W. Ji, C. Arnst, A. R. Tipton, M. E. Bekier II, W. R. Taylor, T. J. Yen, S.-T. Liu, OTSSP167 abrogates mitotic checkpoint through inhibiting multiple mitotic kinases. *PLOS ONE* **11**, e0153518 (2016). doi: 10.1371/journal.pone.0153518; Medline
- 115. B. B. Touré, J. Giraldes, T. Smith, E. R. Sprague, Y. Wang, S. Mathieu, Z. Chen, Y. Mishina, Y. Feng, Y. Yan-Neale, S. Shakya, D. Chen, M. Meyer, D. Puleo, J. T. Brazell, C. Straub, D. Sage, K. Wright, Y. Yuan, X. Chen, J. Duca, S. Kim, L. Tian, E. Martin, K. Hurov, W. Shao, Toward the validation of maternal embryonic leucine zipper kinase: Discovery,

- optimization of highly potent and selective inhibitors, and preliminary biology insight. *J. Med. Chem.* **59**, 4711–4723 (2016). doi: 10.1021/acs.jmedchem.6b00052; Medline
- 116. S. Chung, K. Kijima, A. Kudo, Y. Fujisawa, Y. Harada, A. Taira, N. Takamatsu, T. Miyamoto, Y. Matsuo, Y. Nakamura, Preclinical evaluation of biomarkers associated with antitumor activity of MELK inhibitor. *Oncotarget* **7**, 18171–18182 (2016). doi: 10.18632/oncotarget.7685; Medline
- 117. L. M. Kelly, Q. Liu, J. L. Kutok, I. R. Williams, C. L. Boulton, D. G. Gilliland, FLT3 internal tandem duplication mutations associated with human acute myeloid leukemias induce myeloproliferative disease in a murine bone marrow transplant model. *Blood* **99**, 310–318 (2002). doi: 10.1182/blood.V99.1.310; Medline
- 118. T. Fischer, R. M. Stone, D. J. DeAngelo, I. Galinsky, E. Estey, C. Lanza, E. Fox, G. Ehninger, E. J. Feldman, G. J. Schiller, V. M. Klimek, S. D. Nimer, D. G. Gilliland, C. Dutreix, A. Huntsman-Labed, J. Virkus, F. J. Giles, Phase IIB trial of oral Midostaurin (PKC412), the FMS-like tyrosine kinase 3 receptor (FLT3) and multi-targeted kinase inhibitor, in patients with acute myeloid leukemia and high-risk myelodysplastic syndrome with either wild-type or mutated FLT3. *J. Clin. Oncol.* 28, 4339–4345 (2010). doi: 10.1200/JCO.2010.28.9678; Medline
- 119. S. Opatz, H. Polzer, T. Herold, N. P. Konstandin, B. Ksienzyk, E. Zellmeier, S. Vosberg, A. Graf, S. Krebs, H. Blum, K. P. Hopfner, P. M. Kakadia, S. Schneider, A. Dufour, J. Braess, M. C. Sauerland, W. E. Berdel, T. Büchner, B. J. Woermann, W. Hiddemann, K. Spiekermann, S. K. Bohlander, P. A. Greif, Exome sequencing identifies recurring *FLT3* N676K mutations in core-binding factor leukemia. *Blood* **122**, 1761–1769 (2013). doi: 10.1182/blood-2013-01-476473; Medline
- 120. K. S. Reiter, H. Polzer, C. Krupka, B. Vick, A. Maiser, M. S. Subklewe, I. Jeremias, H. Leonhardt, K. Spiekermann, P. A. Greif, Tyrosin kinase inhibition restores the membrane localization of FLT3-ITD. *Blood* **126**, 1274 (2015).
- 121. V. B. Chen, W. B. Arendall III, J. J. Headd, D. A. Keedy, R. M. Immormino, G. J. Kapral, L. W. Murray, J. S. Richardson, D. C. Richardson, *MolProbity*: All-atom structure validation for macromolecular crystallography. *Acta Crystallogr. D Biol. Crystallogr.* **66**, 12–21 (2010). doi: 10.1107/S0907444909042073; Medline

- 122. P. D. Adams, P. V. Afonine, G. Bunkóczi, V. B. Chen, I. W. Davis, N. Echols, J. J. Headd, L.-W. Hung, G. J. Kapral, R. W. Grosse-Kunstleve, A. J. McCoy, N. W. Moriarty, R. Oeffner, R. J. Read, D. C. Richardson, J. S. Richardson, T. C. Terwilliger, P. H. Zwart, *PHENIX*: A comprehensive Python-based system for macromolecular structure solution. *Acta Crystallogr. D Biol. Crystallogr.* **66**, 213–221 (2010). doi: 10.1107/S0907444909052925; Medline
- 123. P. Arreba-Tutusaus, T. S. Mack, L. Bullinger, T. M. Schnöder, A. Polanetzki, S. Weinert, A. Ballaschk, Z. Wang, A. J. Deshpande, S. A. Armstrong, K. Döhner, T. Fischer, F. H. Heidel, Impact of FLT3-ITD location on sensitivity to TKI-therapy in vitro and in vivo. *Leukemia* **30**, 1220–1225 (2016). doi: 10.1038/leu.2015.292; Medline